Advances in Mathematical Sciences and Applications
Vol. 30, No. 2 (2021), pp. 521– 554

GAKKOTOSHO
TOKYO JAPAN

MULTI-COMPONENT RED BLOOD CELL COMPUTATIONAL MODELING: A NEW MATHEMATICAL FORMULATION

With gratitude to the Institute of Mathematics and Computer Sciences of the University of São Paulo in São Carlos (SP), Brazil

Luca Meacci

Instituto de Ciências Matemáticas e de Computação
Universidade de São Paulo, São Carlos (SP), Brazil
(E-mail: luca.meacci@usp.br)

Roberto Federico Ausas

Instituto de Ciências Matemáticas e de Computação
Universidade de São Paulo, São Carlos (SP), Brazil
(E-mail: rfausas@icmc.usp.br)

Fernando Mut

Bioengineering Department
George Mason University, Fairfax (VA), USA
(E-mail: fmut@gmu.edu)

and

Gustavo Carlos Buscaglia

Instituto de Ciências Matemáticas e de Computação
Universidade de São Paulo, São Carlos (SP), Brazil
(E-mail: gustavo.buscaglia@icmc.usp.br)

Communicated by Mario Primicerio; Received september 30, 2021.
This work is supported by INCT-MACC (Instituto Nacional de Ciência e Tecnologia - Medicina Assistida por Computação Científica), approved from CNPq (Conselho Nacional de Desenvolvimento Científico e Tecnológico) of Brazil and financed by FAPESP (Fundação de Amparo à Pesquisa do Estado de São Paulo) of Brazil (Grant 2014/50889-7). This research was developed making use of the computational resources (Euler cluster) of the CeMEAI (Center for Mathematical Sciences Applied to Industry) financed by FAPESP of Brazil (Grant 2013/07375-0).
AMS Subject Classification: 76Zxx, 74F10, 74L15, 92Cxx.
Keywords: Red blood cell, Mathematical modelling, Biological fluid mechanics, Lipid membrane, cytoskeleton, Fluid-solid interactions.

Abstract.

In this article, we present a new mathematical/computational formulation for a multicomponent model to study the normal and pathological behaviour of red blood cells in slow transient processes. We take into account (i) the lipid bilayer behaviour, (ii) the cytoskeleton dynamics, (iii) the interaction activity between them, and (iv) the internal cytoplasm flow. The formulation considers the cytoskeleton as a discrete non-linear elastic structure. The first novelty is to couple it with continuum models of the lipid membrane and of the cytoplasm, instead of the usual discrete/particle models. The second novelty is that the interaction of the cytoskeleton with the membrane is through adhesion forces adapted from efficient solid-solid adhesion algorithms. The model is tested with virtual experiments such as relaxation towards equilibrium and stretching by optical tweezers.

1 Introduction

In recent years, a multi-component approach in red blood cell (RBC) mathematical/computational modeling has been taking hold as new formulations and techniques have been introduced. The biological motivation hinges on the same RBC composite architecture. During its 120 days average life cycle, the RBC is subjected to strong stresses and deformations, as it traverses the human circulatory system in capillaries of the order of magnitude of its own size. Its ability to deform and assume the typical biconcave shape again is closely connected with its physiological function of transporting oxygen to tissues and organs. Hence, the need to consider the contribution of each component of the erythrocyte structure to simulate the mechanical behavior exhaustively.

The human RBC physiognomy is rich and complex [1], but could be simplified for our modeling objectives, as shown in Figure 1. With an average width of $7.5\,\mu m$ and height of $2\,\mu m$, the RBC is surrounded by a double layer made of phospholipid molecules (in yellow in Figure 1), called lipid bilayer of $5\,nm$ of thickness. This cellular membrane is complemented by a cytoskeleton, which contributes to the flexibility and stability of the cell. Such network consists of long twisted strands of spectrin and actin filaments (in Figure 1 colored in purple). Transmenbranic proteins allow the cytoskeleton to attach (and detach) to the bilayer, contributing to an interactional adhesion between the two components. Finally, the cytoplasm (in green in Figure 1) is the part of the cell which is contained within the entire cell membrane. It is essentially a fluid composed of cytosol and organelles and rich in hemoglobin, an iron-containing biomolecule that can bind oxygen. In the RBC case, the nucleus is absent so that it can contain more haemoglobin to increase oxygen carry capacity.

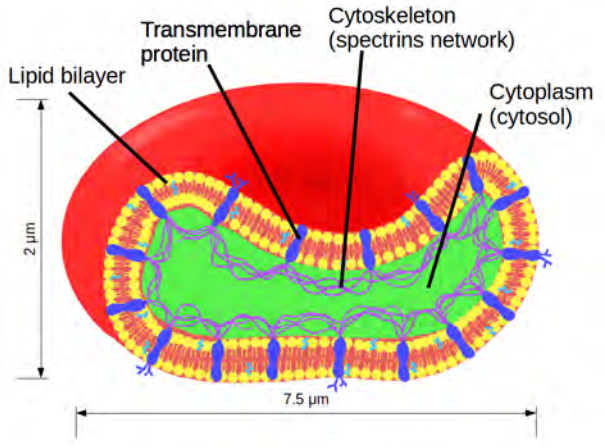

Figure 1: RBC main components structure. The illustration is produced by Arantxa Deneb Gómez Pirela

It is a difficult task to succeed in synthesizing the multiple approaches adopted to try to mimic mechanical behavior. All of them have strengths and elements of weakness [2]. Some reviews are been presented illustrating a general discussion of numerical simulation challenges of flowing blood cells [3, 4]. However, we can opt to divide them into two large classes: continuum-based and particle-based models. We propose in Table 1 a

schematic overview and summary of the contributions that in some way represent the best practices that have contributed to growth in the field of mathematical/computational RBC modeling, and from which other works have followed. Continuum-based models arise naturally when one aspires to describe fluid-structure interactions between the RBCs and the surrounding flow. They have the advantage to benefit from the experience of the well-established continuum mechanics community and of robust and accurate numerical methods [5]. Some of them are represented by the implementation of boundary integral method (BIM) [6, 7] and immersed boundary method (IBM) [8, 9]. In the case of simple shear flows, they can be successfully adopted. On the other hand, particle-based models, which treat both the fluid and the cell membrane as particulate materials, can easier take into account the non-homogenuos RBC structure, introducing elements like cytoskeleton spectrins, proteins, defects, and so on [10]. Nonetheless, although coarse-grained methods are eligible, they usually are computationally very expensive for large-scale applications. This class represents a very extensive field to which Multi-particle collision dynamics (MPCD) method [11, 12], coarse-grained molecular dynamics (CGMD) techniques [13] and dissipative particle dynamics (DPD) methods [14, 15, 16, 17] belong. They also reflect the choice of some most recent and complete works for the whole cell study, consisting in OpenRBC code [18] and LAMMS molecular dynamics simulator [19]. A special mention deserves the work of Peng et al. (2010, 2011) [20, 21], for having well focused the idea that, to model a RBC, an holistic vision on several levels is necessary. In addition, the cytoskeleton is a component that has acquired space with dedicated studies. A common choice in this direction is to adopt nonlinear elastic models of the worm-like chain type. Finally, we aim to highlight approaches that use the curvature concept according to the Camnhan-Helfrich model [22, 23, 24]. This assumption allows a continuous description of the lipid bilayer and consequently lends itself to the use of efficient numerical methods such as the finite element method (FEM). From this idea, very recently our group of authors presented a two-component model that mimics the behavior of the lipid bilayer, the cytoskeleton, and the interaction dynamics between the two parts [25, 26].*

The developments of various mathematical formulations and complementary numerical techniques have led to continuous improvements and an ever-increasing differentiation of the contributions of the various RBC components. The novelty of this work is to consider a full-component model, i.e., simulating (i) the lipid bilayer behavior, (ii) the cytoskeleton dynamics, (iii) the interaction activity between them, and (iv) the internal cytoplasm flow. In a previous work, the authors justified the choice and the advantage to adopt the continuum approach for membrane modeling; this new multi-components mathematical formulation is presented and achieved based on the same line. The availability of the model is tested with virtual experiments such as resting shape process, optical tweezers stretching, and micropipette aspiration.

The remainder of this paper is organized as follows. The Section 2 concern the detailed mathematical abstraction of the model, considering the various components and pointing out the cytoplasm fluid introduction. In Section 3 we present the suitability of the model to simulate classical RBC experiments and we provide some considerations of discussion. Finally, in the Section 4, we summarize the article achievements and we suggest future

*We remark that another topic is the active nature of RBC flickering and thermal fluctuations of the membrane; this subject, although of interest, is beyond the scope of this work [27].

Table 1: Comparative summary review of RBC component models (best practices).

RBC Model	Authors Year Reference	Components LB CD AI IF	Method	Applications
Membrane BIM continuum-based	Ramanujan & Pozrikidis (1998) [6] Veerapaneni et al. (2011) [7]	⋆	Boundary integral method	Shear flows
Membrane IBM continuum-based	Yazdani & Bagchi (2011) [8] Heintz (2015) [9]	⋆ ⋆	Immersed boundary method	Shear flows Viscous fluid embedded
Membrane curvature-based	Arroyo & DeSimone (2009) [22] Barrett et al. (2015) [23] Rodrigues et al. (2015) [24]	⋆	Canham-Helfrich model	Curvature model Shape transitions Tethering
Mechanical deformation	Dao et al. (2003) [28]	⋆ ⋆	Continuum mechanics	Optical tweezers Simulations with cytosol
Cytoskeleton network	Boey et al. (1998) [29] Discher et al. (1998) [30]	⋆	Worm-like chain model	Large Deformation Micropipette aspiration
Two-component MPCD	Noguchi & Gompper (2005) [11] McWhirter et al. (2009) [12]	⋆	Multi-particle collision dynamics Stochastic rotation dynamics	Shape transitions Tube flow
One-component DPD	Pivkin & Karniadakis (2008) [14] Fedosov et al. (2010) [15]	⋆	Dissipative particle dynamics	Whole cell level Tube flow
Two-component CGMD	Li & Lykotrafitis (2012) [13]	⋆ ⋆	Coarse-grained molecular dynamics	One portion membrane Membrane vesiculation Transmembrane protein
Three-level multiscale	Peng et al. (2010, 2011) [20, 21]	⋆ ⋆	Continuum mechanics	Multiscale analysis Whole cell level Stokes flow
Two-component DPD model	Peng et al. (2013) [16] Li & Lykotrafitis (2014) [17]	⋆ ⋆ ⋆	Dissipative particle dynamics	Cyto-bilayer interaction Optical tweezers
OpenRBC	Tang et al. (2017) [18]	⋆ ⋆ ⋆	Coarse-grained molecular dynamics	Whole cell level Cyto-bilayer interaction
LAMMPS	Fu et al. (2017) [19]	⋆ ⋆ ⋆ ⋆	Coarse-grained molecular dynamics	Shape transition Resting shapes
Two-component continuum-based	Meacci et al. (2020) [25, 26]	⋆ ⋆ ⋆	Canham-Helfrich model Worm-like chain	Shape transition Cyto-bilayer interaction

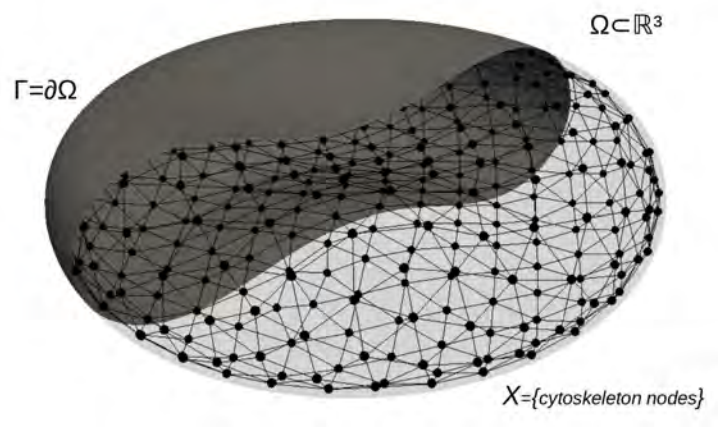

Figure 2: Mathematical domain of the model.

applications of the model.

2 Methods and Models

We suppose that from the mathematical point of view, a RBC is a domain $\bar{\Omega} \subset \mathbb{R}^3$. The frontier $\partial\Omega$ models the lipid bilayer and we denote it with Γ. The inside of the domain Ω is filled with a fluid of constant viscosity μ_f, to simulate the cytoplasm. The bilayer receives an interaction force from the cytoskeleton, this is in the real system through the possible anchoring to the transmenbranic proteins. In our abstraction process, this adhesion form is mimicked with a potential defined *ad hoc*. Finally, the cytoskeleton is schematized as a set $\boldsymbol{X}$ of N_X nodes connected to each other by elastic links. We can see a representation of such a domain in Figure 2.

2.1 Virtual work principle

We aim to describe the motion of $\bar{\Omega} \subset \mathbb{R}^3$ under the action of viscoelastic and external forces. We opt for the application of the virtual work principle [31], that in our case reads

$$\int_{\bar{\Omega}} \boldsymbol{\Sigma} \,:\, D\boldsymbol{z} = -d\mathcal{E}_\Gamma(\boldsymbol{z}) + \int_{\bar{\Omega}} \boldsymbol{f} \cdot \boldsymbol{z}, \quad \forall \boldsymbol{z} \in \boldsymbol{Z}, \tag{1}$$

being $\boldsymbol{\Sigma}$ the tangential stresses tensor, $\mathcal{E}_\Gamma$ the elastic membrane energy, $\boldsymbol{f}$ in the net interaction force with the surroundings, $\boldsymbol{Z}$ the space of virtual admissible velocities, and $D\boldsymbol{z}$ the virtual strain rate. The left side of (1) is the dissipation term due to the motion/deformation of Γ, while $d\mathcal{E}_\Gamma(\boldsymbol{z})$ denotes the first variation of $\mathcal{E}_\Gamma$ along the virtual velocity field $\boldsymbol{Z}$.

The mathematical formulation (1) is very concise and therefore efficient. We consider one unique domain $\bar{\Omega}$ to describe the cytoplasmatic internal fluid and the lipid bilayer, being it simply its border. This fact implies that we can use one only *velocity field* $\boldsymbol{W} = \{\boldsymbol{w} \,|\, \boldsymbol{w} : \bar{\Gamma} \to \mathbb{R}^3\}$ to describe, for a given time instant, the configuration of both components. Although we have one only variable $\boldsymbol{w} \in \boldsymbol{W}$, however, the equations are

defined according to the domain zone, as it happens for example in the case of dissipation where we split the different contributions of the internal fluid and external membrane. Furthermore, the integral over $\boldsymbol{f}$ contains not only external forces but also the contribution in the form of interaction of the cytoskeleton to the bilayer. This explicit description implicitly requires the formulation of the cytoskeleton dynamics. In the following sections, we provide step-by-step the complete mathematical model, introducing assumptions and detailing the components.

2.2 Dissipation and Boussinesq-Scriven law

As previously mentioned, we divide the dissipation term into 2 parts

$$\int_{\bar{\Omega}} \boldsymbol{\Sigma} \,:\, D\boldsymbol{z} = \int_{\Gamma} \boldsymbol{\Sigma}_{\boldsymbol{\Gamma}} \,:\, D_{\Gamma}\boldsymbol{z} + \int_{\Omega} \boldsymbol{\Sigma} \,:\, D\boldsymbol{z}. \tag{2}$$

Let us focus firstly on the term concerning the lipid bilayer. It is preliminarily necessary to introduce some notations and surface differential operators. For further information, we suggest to consult the works of Buscaglia & Ausas [32] and Biria et al. [33]. Nonetheless, in this paper, we refer to the analog of the common symmetric gradient $D\boldsymbol{z} = (\nabla\boldsymbol{z} + \nabla\boldsymbol{z}^T)/2$ to indicate the corresponding surface operator

$$D_{\Gamma}\boldsymbol{z} = \frac{1}{2}\mathbb{P}(\nabla_{\Gamma}\boldsymbol{z} + \nabla_{\Gamma}\boldsymbol{z}^T)\mathbb{P} \tag{3}$$

where the the tensor $\mathbb{P}$ is the *tangential projector* onto the surface Γ,

$$\mathbb{P} = \mathbb{I} - \check{\boldsymbol{n}} \otimes \check{\boldsymbol{n}}, \tag{4}$$

$\check{\boldsymbol{n}}$ is the outward normal vector to Γ, and ∇_{Γ} is the *tangential or surface gradient operator*, defined as

$$\nabla_{\Gamma} g = \mathbb{P}\,\nabla\widehat{g}, \tag{5}$$

with $g : \Gamma \to \mathbb{R}$ is any function and $\widehat{g}$ an arbitrary extension of g to an open neighborhood of $\Gamma \subset \mathbb{R}^3$. We remark that the corresponding *surface Laplacian* $\Delta_{\Gamma} g$ is given by $\nabla_{\Gamma} \cdot (\nabla_{\Gamma} g)$. Finally, the surface gradient of a vector, as in the case of $\nabla_{\Gamma}\boldsymbol{z}$ in equation (3) is a matrix as follows

$$\{\nabla_{\Gamma}\boldsymbol{z}\}_{ij} = \{\,\nabla_{\Gamma} z_i\}_j, \tag{6}$$

being w_i the i-th $\boldsymbol{z}$ component.

Once these geometrical and differential preliminaries are established, we introduce the costitutive law for the rheology of the viscous interface. According to the *Boussinesq-Scriven law* [34, 35, 36], the stress tensor related to Γ is given by

$$\boldsymbol{\Sigma}_{\boldsymbol{\Gamma}} \;=\; (-p_S + \lambda\nabla_{\Gamma}\cdot\boldsymbol{w})\mathbb{P} + 2\,\mu\, D_{\Gamma}\boldsymbol{w}, \tag{7}$$

where λ and μ are surface viscosity coefficients, and p_S is a surface thermodynamic pressure that requires a closure law. We assume also that the bilayer is an *inextensible membrane*, i.e. an area-preserving interface. Therefore, the condition of inextensibility holds

$$\nabla_{\Gamma}\cdot\boldsymbol{w} = 0. \tag{8}$$

Under the constraint (8), making λ tend to infinity, we obtain the classical result that there exists a *surface tension* σ such that $\lim_{\lambda\to+\infty}(-p_S + \lambda\nabla_\Gamma \cdot \boldsymbol{w}) = \sigma$. Consequently, for an inextensible membrane, we have a closure law for p_S and the (7) becomes

$$\boldsymbol{\Sigma_\Gamma} \;=\; \sigma\,\mathbb{P} + 2\,\mu\,D_\Gamma \boldsymbol{w}. \tag{9}$$

That means that finally we can write the dissipation term for Γ as follows

$$\int_\Gamma \boldsymbol{\Sigma_\Gamma} \;:\; D_\Gamma \boldsymbol{z} \;=\; \int_\Gamma 2\,\mu\,D_\Gamma \boldsymbol{w} \;:\; D_\Gamma\,\boldsymbol{z} \;+\; \int_\Gamma \sigma \nabla_\Gamma \cdot \boldsymbol{z}. \tag{10}$$

Let us now consider the dissipation term of 2, concerning the internal bulk fluid of Ω. In this case, the classical Newtonian law [37] reads

$$\boldsymbol{\Sigma} \;=\; (\lambda_f \nabla_\Gamma \cdot \boldsymbol{w})\mathbb{I} + 2\,\mu_f\,D\boldsymbol{w}, \tag{11}$$

where, λ_f and μ_f are fluid viscosity coefficients, and $\mathbb{I}$ is the identity tensor (identity matrix). Similarly to the previous case, we apply the incompressibility condition for the fluid i.e., $\nabla \cdot \boldsymbol{w} = 0$. By tending λ_f to infinity we can introduce the variable internal *fluid pressure* p, obtaining the explicit description of the dissipative term for the fluid

$$\int_\Omega \boldsymbol{\Sigma} \;:\; D\boldsymbol{z} = \int_\Omega 2\,\mu_f\,D\boldsymbol{w} \;:\; D\boldsymbol{z} \;+\; \int_\Omega p\nabla \cdot \boldsymbol{z}. \tag{12}$$

which is the weak form of the usual result of the Stokes equations $-\mu_f \Delta \boldsymbol{w} + \nabla p$.

2.3 Laplace-Beltrami identity and Canham-Helfrich energy

We introduce one more variable, the *mean curvature vector* $\boldsymbol{\kappa}$; it is equals to $H\,\boldsymbol{n}$, with H the mean curvature), which defines a field over Γ. The geometrical equation for $\boldsymbol{\kappa}$ satisfies the *Laplace-Beltrami identity* $-\Delta_\Gamma \boldsymbol{\chi} = \boldsymbol{\kappa}$ that in weak form is

$$\int_\Gamma \boldsymbol{\kappa} \cdot \boldsymbol{\zeta} = \int_\Gamma \nabla_\Gamma \boldsymbol{\chi} \cdot \nabla_\Gamma \boldsymbol{\zeta} = \int_\Gamma \mathbb{P} : \nabla_\Gamma \boldsymbol{\zeta}, \quad \forall \boldsymbol{\zeta} \in L^2(\Gamma) \tag{13}$$

where $\boldsymbol{\chi}$ is the identity mapping on Γ, i.e., $\boldsymbol{\chi}(\boldsymbol{x}) = \boldsymbol{x}, \forall \boldsymbol{x} \in \Gamma$, and $\nabla_\Gamma \boldsymbol{\chi} = \mathbb{P}$.

The intrinsic bilayer energy $\mathcal{E}_-$ is assumed to obey the *Canham-Helfrich model* [38, 39], according to

$$\mathcal{E}_\Gamma = \frac{c_{\text{CH}}}{2} \int_\Gamma \|\boldsymbol{\kappa}\|^2. \tag{14}$$

We are interested in explicitly evaluating the term $d\mathcal{E}_\Gamma(\boldsymbol{z})$ of equation (1), that is the $\mathcal{E}$ variation as a consequence of a perturbation of the bilayer shape along a vector field $\boldsymbol{z}$ defined on Γ. We recall that the *shape derivative* of a functional $\mathcal{I}$ in the direction of a virtual vector field $\boldsymbol{z}$ is defined as $d\mathcal{I}(\boldsymbol{z})(\boldsymbol{x}) = \lim_{\epsilon\to 0} \frac{\mathcal{I}(\boldsymbol{x}+\epsilon\boldsymbol{z}) - \mathcal{I}(\boldsymbol{x})}{\epsilon}$ where $\boldsymbol{x} \in \Gamma$. When the (14) holds, with some calculations (see [40, 24]) we obtain

$$d\mathcal{E}_\Gamma(\boldsymbol{z}) = c_{\text{CH}} \int_\Gamma \left[\nabla_\Gamma \boldsymbol{\kappa} : \nabla_\Gamma \boldsymbol{z} - \nabla_\Gamma \boldsymbol{z} (\nabla_\Gamma \boldsymbol{\chi} + \nabla_\Gamma \boldsymbol{\chi}^T) : \nabla_\Gamma \boldsymbol{\kappa} + \frac{1}{2} (\nabla_\Gamma \cdot \boldsymbol{\kappa})\,(\nabla_\Gamma \cdot \boldsymbol{z}) \right] \tag{15}$$

or equivalently, with respect to the tangential projector, the (15) can be written as

$$d\mathcal{E}_\Gamma(\boldsymbol{z}) = c_{\text{CH}} \int_\Gamma \left[(\mathbb{I} - 2\,\mathbb{P}) \nabla_\Gamma \boldsymbol{\kappa} : \nabla_\Gamma \boldsymbol{z} + \frac{1}{2} (\nabla_\Gamma \cdot \boldsymbol{\kappa})\,(\nabla_\Gamma \cdot \boldsymbol{z}) \right] , \tag{16}$$

that finally we consider in the formulation of our model.

2.4 Inextensible membrane and osmotic equilibrium constraints

Because of (8), the *tangential motion* may be *area preserving*, being $\frac{d\mathcal{A}}{dt} = \int_\Gamma \nabla_\Gamma \cdot \boldsymbol{w} = 0$. In discrete time, nevertheless, this condition is not satisfied exactly; $\mathcal{A}$ can shift from the correct value $\mathcal{A}^*$. For numerical purposes, the area restriction can be therefore implemented as

$$\int_\Gamma \nabla_\Gamma \cdot \boldsymbol{w} \;=\; \frac{\mathcal{A}^* - \mathcal{A}(t)}{\tau_{\mathcal{A}}\, \mathcal{A}(t)} \;, \tag{17}$$

in order to force $\mathcal{A}(t)$ to the $\mathcal{A}^*$ value with the characteristic time $\tau_{\mathcal{A}}$.

Similarly, for the volume, the osmotic equilibrium establishes that the *enclosed volume* may be fixed to a $\mathcal{V}^*$ value. $\int_\Gamma \boldsymbol{w}\cdot\boldsymbol{n}\, d\Gamma = 0 \Rightarrow \frac{d\mathcal{V}}{dt} = \int_\Gamma \boldsymbol{w}\cdot\boldsymbol{n}\, d\Gamma = 0$. However, similarly to the area case we set

$$\int_\Omega \boldsymbol{w}\cdot\boldsymbol{n} \;=\; \frac{\mathcal{V}^* - \mathcal{V}(t)}{\tau_{\mathcal{V}}\, \mathcal{V}(t)} \;, \tag{18}$$

where $\tau_{\mathcal{V}}$ is the characteristic time to force $\mathcal{V}(t)$ to $\mathcal{V}^*$.

The Lagrange multipliers are the surface tension field and pressure field spaces (Boyle law), for the volume and area restrictions, respectively.

2.5 Cytoskeleton component

The remarkable RBC mechanical properties are largely attributed to its cytoskeleton [41]. To subsequently quantify the cytoskeleton interaction with the lipid membrane, we briefly provide a model for such a component. We can treat the cytoskeleton by following the nature of its components, basically a spectrin fiber network with special joints [42, 43]. The typical length of a spectrin filament is $70nm$, leading to about 10^5 edges for a single RBC. This number, even large, is numerically treatable. In addition, coarse-grained models have been developed to save computing effort [14]. For a comprehensive review of RBC cytoskeleton modeling details, we refer the reader to [44]. As yet displayed in the Figure 2, mathematically we can consider for the nodes a set of vertex points $X = \{\boldsymbol{X}^j \mid \boldsymbol{X}^j \in \mathbb{R}^3 \subset \Omega,\ \text{with } j = 1\ \ldots\ N_X\}$ which forms a two-dimensional network of triangles. The model considers this mesh made of a set of nodes (junctions) joined by N_e molecular chains (edges) represented by worm-like chains [45, 46].

In accordance with these preamble considerations, the elastic cytoskeleton mesh energy $\mathcal{E}_X$ can be read as

$$\mathcal{E}_X = \sum_j \left[\frac{k_B T \ell_m \,(3x_j^2 - 2x_j^3)}{4\ell_p(1 - x_j)} + \frac{k_p}{\ell_j} \right] \tag{19}$$

where ℓ_j is the filament length j, ℓ_m is the maximum extension of these filaments, $x_j = \ell_j/\ell_m$, ℓ_p is the persistence length, $k_B T$ is the unit of energy and k_p is a parameter. We remark that the first term in the equation(19) is the pure worm-like chain (WLC) attractive potential, while the second term is related to a repulsive force, called power force (POW). This is the reason why some authors refer to this approach as WLC-POW model [15].

By differentiating (19) with respect to the vector of nodal coordinates, we can obtain the cytoskeleton force $\mathbf{F}^j$ on the j-th node. We remark that the real equations governing

the cytoskeleton movement are $m\,\frac{d^2\mathbf{X}^j}{dt^2} + \frac{\partial \mathcal{E}_X}{\partial \mathbf{X}^j} = \mathbf{F}^j$, where m denotes the effective mass of each node. However, the inertia is very small at the scale of the junction complexes, so that for the mathematical formulation we adopt $m = 0$, i.e.,

$$\mathbf{F}^j = \frac{\partial \mathcal{E}_X}{\partial \mathbf{X}^j} \ . \tag{20}$$

From a numerical point of view, nevertheless, the complete equations are normally numerically integrated with an implicit Newmark scheme, which is well established in solid mechanics.

2.6 Cytoskeleton-bilayer interaction

The interaction between the membrane and the skeleton mimics the adhesion between these two components and the corresponding mutual transmission of mechanical properties. It deserves particular attention and is the last element for the closure of the mathematical formulation of the model. In particular, since we hypothesize that there are no other external forces onto Ω, we define the last term of the right-hand side of the (1). For this goal, we benefit from recent progress on the computational modeling of the adhesion of soft bodies, adapting the formulation of Sauer [47] (see also [48, 49, 50, 16]).

Let us denote by Υ *the adherent surface* of the cytoskeleton. The general form for the contact energy $\mathcal{E}_{con}$ is given by

$$\mathcal{E}_{con} = \int_\Gamma \int_\Upsilon \beta_\Gamma \ \beta_\Upsilon \ \phi(\|\mathbf{x}^\Gamma - \mathbf{x}^\Upsilon\|) \ d\mathbf{x}^\Gamma \ d\mathbf{x}^\Upsilon \tag{21}$$

where ϕ is the interaction potential (in Joule/m^4) and β_Γ, β_Υ are dimensionless scalars. In many applications, mathematical modelers are used to opt for the Lennard-Jones potential [51], i.e., $\phi(d) = \varepsilon \left(\frac{r_0}{d}\right)^k - 2\varepsilon \left(\frac{r_0}{d}\right)^{k/2}$, where d is the distance between two particles and, r_0 and ε are length and energy scales, respectively. This potential has a minimum of value $-\varepsilon$ at $d = r_0$, it is repulsive for $d < r_0$ and attractive if $d > r_0$.

The contact force on the bilayer resulting from this energy therefore consists in

$$\mathbf{f}^{\,\mathrm{con},\Gamma}(\mathbf{x}^\Gamma) = -\,\beta_\Gamma \int_\Upsilon \beta_\Upsilon \phi'(\|\mathbf{x}^\Gamma - \mathbf{x}^\Upsilon\|) \, \frac{\mathbf{x}^\Gamma - \mathbf{x}^\Upsilon}{\|\mathbf{x}^\Gamma - \mathbf{x}^\Upsilon\|} \ d\mathbf{x}^\Upsilon \ . \tag{22}$$

Attributing a spherical shape of radius R and center $\mathbf{c}$ to Υ, this integral can be computed analytically as an explicit function $\mathcal{G}(\|\mathbf{x}^\Gamma - \mathbf{c}\| - R, r_0, \varepsilon)$ times the unit vector along $\mathbf{x}^\Gamma - \mathbf{c}$. The function $\mathcal{G}$ diverges when $d = \|\mathbf{x}^\Gamma - \mathbf{c}\| - R$ tends to 0, since $d < 0$ implies interpenetration. To improve the numerical resolution, the authors recently proposed a variation of the regularized potential [25]. In a complementary manner, the force exerted on a point x^Υ of the adherent surface of the cytoskeleton by the bilayer Γ is given by

$$\mathbf{f}^{\,\mathrm{con},\Upsilon}(\mathbf{x}^\Upsilon) = \ \beta_\Upsilon \int_\Gamma \beta_\Gamma \phi'(\|\mathbf{x}^\Gamma - \mathbf{x}^\Upsilon\|) \, \frac{\mathbf{x}^\Gamma - \mathbf{x}^\Upsilon}{\|\mathbf{x}^\Gamma - \mathbf{x}^\Upsilon\|} \ d\mathbf{x}^\Gamma \ . \tag{23}$$

As we expected from the action-reaction principle, $\int_\Gamma \mathbf{f}^{\,\mathrm{con},\Gamma} + \int_\Upsilon \mathbf{f}^{\,\mathrm{con},\Upsilon} = 0$. For a more detailed exposition of the formulation and calculations, the authors recently presented a

paper [26]. The contact force only acts along the surface normal. For this reason, it is complemented by a drag force that models the tangential attachment of the citoskeleton nodes to the bilayer anchoring proteins as

$$\mathbf{f}^{d,\Gamma}(\mathbf{x}^\Gamma) = -\int_\Upsilon \eta \left(\mathbf{w}(\mathbf{x}^\Gamma) - \frac{d\mathbf{x}^\Upsilon}{dt}\right)\, d\mathbf{x}^\Upsilon, \qquad \mathbf{f}^{d,\Upsilon}(\mathbf{x}^\Upsilon) = \int_\Gamma \eta \left(\mathbf{w}(\mathbf{x}^\Gamma) - \frac{d\mathbf{x}^\Upsilon}{dt}\right)\, d\mathbf{x}^\Gamma, \tag{24}$$

where η is a drag coefficient that depends on $\|\mathbf{x}^\Gamma - \mathbf{x}^\Upsilon\|$. We highlight that the set $\{\mathbf{X}^i\}_{i=1}^{N_X}$ concerns the coordinates of the centers of the nodes, while Υ consists of spheres Υ^j of a given radius around $\mathbf{X}^j$, i.e., the surfaces of the junctions. The net force per unit area acting on the bilayer is thus $\mathbf{f}^\Gamma = \mathbf{f}^{\,\mathrm{con},\Gamma} + \mathbf{f}^{d,\Gamma}$, while the net force on node j, to be equilibrated by the worm-like chains, according to the (20), is

$$\mathbf{F}^j = \int_{\Upsilon^j} \left(\mathbf{f}^{\,\mathrm{con},\Upsilon}(\mathbf{x}^\Upsilon) + \mathbf{f}^{\,d,\Upsilon}(\mathbf{x}^\Upsilon)\right)\, d\mathbf{x}^\Upsilon\ . \tag{25}$$

2.7 Model summary

We now are able to sum all components to obtain the model mathematical formulation for the RBC configuration at a given instant time. We arrive at the following problem:

Stationary full model problem. Find $(\boldsymbol{w}, \sigma, \boldsymbol{\kappa}, p) \in \boldsymbol{W} \times Q \times \boldsymbol{K} \times \mathcal{P}$ such that

$$\int_\Omega 2\mu_f D\boldsymbol{w} : D\boldsymbol{z} - \int_\Omega p\,\nabla\cdot\boldsymbol{z} + \int_\Gamma 2\,\mu\, D_\Gamma \boldsymbol{w} : D_\Gamma \boldsymbol{z} \;+\; \int_\Gamma \sigma \nabla_\Gamma \cdot \boldsymbol{z} \;+$$
$$+\; c_{\mathrm{CH}} \int_\Gamma \left[(\mathbb{I} - 2\,\mathbb{P})\nabla_\Gamma \boldsymbol{\kappa} : \nabla_\Gamma \boldsymbol{z} + \frac{1}{2}(\nabla_\Gamma \cdot \boldsymbol{\kappa})\,(\nabla_\Gamma \cdot \boldsymbol{z})\right] = \int_\Gamma \boldsymbol{f}^{\,\mathrm{con},\Gamma} \cdot \boldsymbol{z} \tag{26}$$

$$\int_\Gamma \xi\, \nabla_\Gamma \cdot \boldsymbol{w} = \frac{\mathcal{A}^* - \mathcal{A}}{\mathcal{A}\,\tau_{\mathcal{A}}} \int_\Gamma \xi \tag{27}$$

$$\int_\Gamma \boldsymbol{\kappa} \cdot \boldsymbol{\zeta} = \int_\Gamma \mathbb{P} : \nabla_\Gamma \boldsymbol{\zeta} \tag{28}$$

$$\int_\Omega q\, \nabla \cdot \boldsymbol{w} = \frac{\mathcal{V}^* - \mathcal{V}}{\mathcal{V}\,\tau_{\mathcal{V}}} \int_\Omega q \tag{29}$$

$$\frac{\partial \mathcal{E}_X}{\partial \mathbf{X}^j} = \int_{\Upsilon^j} \left(\mathbf{f}^{\,\mathrm{con},\Upsilon}(\mathbf{x}^\Upsilon) + \mathbf{f}^{\,d,\Upsilon}(\mathbf{x}^\Upsilon)\right)\ , \quad j = 1, \ldots, N_x \tag{30}$$

with,

$$\mathcal{E}_X \;=\; \sum_{k=1}^{N_e} \left[\frac{k_B T \ell_m\,(3(x_k)^2 - 2(x_k)^3)}{4\ell_p(1-x_k)} + \frac{k_p}{\ell_k}\right], \quad x_k = \ell_k/\ell_m \tag{31}$$

$$\mathbf{f}^{\,\mathrm{con},\Gamma}(\mathbf{x}^\Gamma) = -\,\beta_\Gamma \int_\Upsilon \beta_\Upsilon \phi'(\|\mathbf{x}^\Gamma - \mathbf{x}^\Upsilon\|)\, \frac{\mathbf{x}^\Gamma - \mathbf{x}^\Upsilon}{\|\mathbf{x}^\Gamma - \mathbf{x}^\Upsilon\|} \tag{32}$$

$$\mathbf{f}^{\,\mathrm{con},\Upsilon}(\mathbf{x}^\Upsilon) = \;\beta_\Upsilon \int_\Gamma \beta_\Gamma \phi'(\|\mathbf{x}^\Gamma - \mathbf{x}^\Upsilon\|)\, \frac{\mathbf{x}^\Gamma - \mathbf{x}^\Upsilon}{\|\mathbf{x}^\Gamma - \mathbf{x}^\Upsilon\|} \tag{33}$$

$$\mathbf{f}^{d,\Upsilon}(\mathbf{x}^\Upsilon) = \int_\Gamma \eta \left(\mathbf{w}(\mathbf{x}^\Gamma) - \frac{d\mathbf{x}^\Upsilon}{dt}\right) \tag{34}$$

$\forall\,(\boldsymbol{z},\xi,\boldsymbol{\zeta},q)\,\in\,\boldsymbol{W}\times Q\times\boldsymbol{K}\times\mathcal{P}$.

Above $\boldsymbol{W}$ is the space of kinematically admissible motions, i.e., essentially $\boldsymbol{W}=\{\boldsymbol{z}:\Omega\to\mathbb{R}^3,\boldsymbol{z}\in C^k$ with k enough large$\}$ with opportune restrictions, such as inextensible and volume-preserving motions. Then $\boldsymbol{K}$ is the mean-curvature-vector space that can be equal to $(H^1(\Gamma))^3$, the space $Q=L^2(\Gamma)$ corresponds to the surface tension field, and $\mathcal{P}=L^2(\Omega)$ is the pressure field space.

Proposition 2.7.1 *Assuming to have computed the cytoskeleton configurations governed by (30) – (30) and related cyto-bilayer contact forces (32) - (34), if*

- Γ *is smooth enough,*
- $\boldsymbol{W}=\{\boldsymbol{z}:\Omega\to\mathbb{R}^3,\boldsymbol{z}\in C^k$ *with* k *enough large*$\}$ *with opportune restrictions,*
- $\boldsymbol{K}=(H^1(\Gamma))^3$,
- $Q=L^2(\Gamma)$,
- $\mathcal{P}=L^2(\Omega)$,

then, the stationary full model problem is well-posed.

Proof. Given a certain configuration of the cytoskeleton (and of the lipid bilayer), we suppose to solve the equations for the cytoskeelton and to calculate the relative contact membrane forces, as assumed in the hypothesis. In the following, we denote with "smoothness" the property to possess a sufficient number of continuous derivatives over the domain. The model solves a composite problem, which can be broken down into parts to prove the well-posedness. Let us proceed in three steps:

(i) We can solve the Laplace-Beltrami equation (28) and find the smooth $\boldsymbol{k}$ solution. It is possible integrating by part the right-hand side of (28) and because Γ, $\boldsymbol{\chi}$ and $\mathbb{P}$ are smooth [52, 53].

(ii) We now neglect the constrains (27) and (29), set $\sigma=p=0$, and substitute the $\boldsymbol{k}$ solution into (26). We obtain essentially 2 bilinear forms;

$$\mathcal{B}_1(\boldsymbol{w},\boldsymbol{z})=\int_\Omega 2\mu_f D\boldsymbol{w}:D\boldsymbol{z}\quad\mathcal{B}_2(\boldsymbol{w},\boldsymbol{z})=\int_\Gamma 2\,\mu\,D_\Gamma\boldsymbol{w}:D_\Gamma\boldsymbol{z}$$

one resolving the Boussinesq-Scriven problem for the velocity w over Γ, and the other one concerning the classical Stokes problem for the velocity w, here in the domain (Ω), respectively. In both cases, it is possible to choose an appropriate space $\boldsymbol{W}\subset H^1(\Omega)^3$ such that the bilinear forms are coercive and therefore $\boldsymbol{W}$ uniquely defined [54]. For example, a possibility is to choose $\boldsymbol{W}$ as the $H^1(\Omega)^3$ quotiented with rigid movements space.

(iii) We finally focus on σ and p. In (27) and (29) the Lagrange multipliers enforce the area and volume preservation. Under these conditions, the existence and uniqueness of these last unknown variables are proved satisfying inf-sup conditions, as yet shown in similar in [24]. It is possible to verify that such requirements are fulfilled by $Q=L^2(\Gamma)$ and $\mathcal{P}=L^2(\Omega)$.

□

2.8 Evolutionary model

In this section, we extend the previous model, which describes the system configuration at a certain fixed time, to the evolutionary dynamics over time. In fact, if the previous case allows to study the model mathematically, from the computation point of view and for simulation purposes, it is crucial to introduce the time dependence. In particular, we denote with $\Omega(t)$ the configuration of the domain Ω at time t and with $X(t) = \{\boldsymbol{X}^j(t) \mid \boldsymbol{X}^j(t) \in \mathbb{R}^3 \subset \Omega(t), \text{ with } j = 1 \ \dots \ N_X\}$ the set of positions of all cytoskeleton nodes at time t. Our evolutionary generalization is expressed with an infinitesimal increase in time, taking into account the families of velocity field over $\Omega(t)$ and of velocity field of the cytoskeleton nodes $Y(t) = \{\boldsymbol{Y}^j(t) \mid \boldsymbol{Y}^j(t) = d\boldsymbol{X}^j(t)/dt, \text{ with } j = 1 \ \dots \ N_X\}$. We lead to the following problem.

Evolutionary model problem. In the presence of known initial configurations $\Omega(0)$ and $X(0)$, compute the evolution of configuration $\Omega(t)$ and $X(t)$, convected by the velocity field arising by solving the stationary full model problem and by choosing the time increment δt such that

$$\forall t, \ \forall \boldsymbol{X}^j(t) \in X(t), \ dist(\boldsymbol{X}^j(t) + \boldsymbol{Y}^j(t)\delta t \, , \boldsymbol{X}^j(t + \delta t)) \leq C_1 \delta t^2 \tag{35}$$

$$\forall t, \ \forall \boldsymbol{x} \in \Gamma(t), \ dist(\boldsymbol{x} + \boldsymbol{w}(\boldsymbol{x}, t)\delta t \, , \Gamma(t + \delta t)) \leq C_2 \delta t^2 \tag{36}$$

for some C_1 and C_2 and where $dist(\cdot, \cdot)$ stands for both point-point and point-surface distance, on a case by case basis.

3 Results/Discussion

In this section, we present the suggested discretization of the model and the methods we use to numerically solve the evolutionary problem. We then show some results.

3.1 Discretization and numerical approach

Following the (35) and (35) assumptions, we define a time increment δt inducing a time distretization so that

$$t_{n+1} = t_n + \delta t, \text{ with } t_0 \text{ given}, \ n = 0, 1, \dots . \tag{37}$$

Let us now proceed to discretize the space domain. The cytoskeleton component is discrete by definition; so we do not need to discretize it. Concerning $\bar{\Omega}$, we have to distinguish the case of the boundary surface Γ which solves the problem of Laplace Beltrami and concerning the Boussinesq-Sciven law from the internal fluid where the velocity and pressure arise by solving a Stokes problem in the three-dimensional domain Ω.

Therefore, concerning Γ we consider triangulation surfaces, which for a fixed mesh connectivity are uniquely described by the triangle vertex position set. The time sequence of triangulation surfaces $\Gamma^0, \Gamma^1, ..., \Gamma^n, ...$ are computed and we define the piecewise affine finite element space

$$P_1^n = \{\boldsymbol{f} \in C^0(\Gamma^n) : \boldsymbol{f}|_K \text{ is affine}, \forall K \text{ triangle in } \Gamma^n\} \tag{38}$$

and with the same Γ^n we consider the approximation spaces for velocity, surface and curvature set as

$$\boldsymbol{W}_h^n = (P_1^n)^3/\boldsymbol{R}, \tag{39}$$
$$Q_h^n = P_1^n, \tag{40}$$
$$\boldsymbol{K}_h^n = (P_1^n)^3, \tag{41}$$

where, as suggested in the previous section, we can opt for $\boldsymbol{R}$ as the rigid movements space, i.e., formally $\boldsymbol{R} = \{\boldsymbol{r} : \mathbb{R}^3 \to \mathbb{R}^3 \,|\, \boldsymbol{r}(\boldsymbol{x}) = \boldsymbol{\omega} \wedge \boldsymbol{x} + \boldsymbol{\beta}, \boldsymbol{\omega}, \boldsymbol{\beta} \in \mathbb{R}^3\}$.

Concerning Ω, we similarly discretize the volume with tetrahedra, in order to obtain a time sequence of tetraized volumes $\Omega^0, \Omega^1, ..., \Omega^n, ...$, where we define the equal order piecewise affine finite element space

$$PV_1^n = \{\boldsymbol{f} \in C^0(\Omega^n) : \boldsymbol{f}|_T \text{ is affine}, \forall\, T \text{ tetrahedron in } \Omega^n\} \tag{42}$$

and the corresponding approximation spaces for the velocity and pressure fields in the volume, i.e.,

$$\boldsymbol{W}_h^n = (PV_1^n)^3/\boldsymbol{R}, \tag{43}$$
$$\mathcal{P}_h^n = PV_1^n. \tag{44}$$

We note that we have used a little abuse of notation for the spaces approximating the velocity, but the meaning, the analogy, and the passage between the superficial and volumetric domain is easy to understand.

We therefore come to the following new discrete problem:

Discrete evolutionary model problem. Update the nodal positions $\mathbf{x}^{\mathbf{i},\mathbf{n}}$ and $\mathbf{X}^{\mathbf{j},\mathbf{n}}$ of the $\bar{\Omega}$ domain (i-th vertex of triangle on Γ or tetrahedron in Ω) and the cytoskeleton (center of the j-th cytoskeleton network node) respectively, according to

$$\mathbf{x}^{i,n+1} = \mathbf{x}^{i,n} + \boldsymbol{w}_h^{i,n+1}(\mathbf{x}^{i,n})\delta t, \tag{45}$$

$$\mathbf{X}^{j,n+1} = \mathbf{X}^{j,n} + \boldsymbol{Y}^{j,n+1}\delta t, \tag{46}$$

such that the velocities $\boldsymbol{w}_h^{i,n+1}$ and $\boldsymbol{Y}^{j,n+1} = (\boldsymbol{X}^{j,t+1} - \boldsymbol{X}^{j,t})/\delta t$ solve the following fully discrete problem, that demands to find $(\boldsymbol{w}_h^{n+1}, \sigma_h^{n+1}, \boldsymbol{\kappa}_h^{n+1}, p_h^{n+1}) \in \boldsymbol{W}_h^n \times Q_h^n \times \boldsymbol{K}_h^n \times \mathcal{P}_h^n$

in such a way that

$$\int_{\Omega^n} 2\mu_f D\boldsymbol{w}_h^{n+1} : D\boldsymbol{z} - \int_{\Omega^n} p_h^{n+1}\,\nabla\cdot\boldsymbol{z} + \int_{\Gamma^n} 2\,\mu\,D_\Gamma \boldsymbol{w}_h^{n+1} : D_\Gamma \boldsymbol{z} \;+\; \int_{\Gamma^n} \sigma_h^{n+1}\nabla_\Gamma\cdot\boldsymbol{z} \;+$$
$$+\; c_{\rm CH}\int_{\Gamma^n}\left[(\mathbb{I}-2\,\mathbb{P})\nabla_\Gamma\boldsymbol{\kappa}_h^{n+1} : \nabla_\Gamma\boldsymbol{z} + \frac{1}{2}(\nabla_\Gamma\cdot\boldsymbol{\kappa}_h^{n+1})\,(\nabla_\Gamma\cdot\boldsymbol{z})\right] = \int_{\Gamma^n}\boldsymbol{f}^{{\rm con},\Gamma,n+1}\cdot\boldsymbol{z}, \quad (47)$$

$$\int_{\Gamma^n}\xi\,\nabla_\Gamma\cdot\boldsymbol{w}^{n+1} \;+\; \int_{\Gamma^n}\gamma_h\,(\nabla_\Gamma\,\sigma_h^{n+1}-\boldsymbol{g}_h^n)\cdot\nabla_\Gamma\xi = \frac{\mathcal{A}^*-\mathcal{A}^n}{\mathcal{A}^n\,\tau_{\mathcal{A}}}\int_{\Gamma^n}\xi, \quad (48)$$

$$\int_{\Gamma^n}\boldsymbol{\kappa}^{n+1}\cdot\boldsymbol{\zeta} - \int_{\Gamma^n}\tau_k\,\nabla_\Gamma\,\boldsymbol{w}_h^{n+1} \;:\; \nabla_\Gamma\boldsymbol{\zeta} = \int_\Gamma \mathbb{P} : \nabla_\Gamma\boldsymbol{\zeta}, \quad (49)$$

$$\int_{\Omega^n} q\,\nabla\cdot\boldsymbol{w}_h^{n+1} + \int_{\Omega^n}\gamma_h^v\,(\nabla p_h^{n+1}-\boldsymbol{h}_h^n)\cdot\,\nabla q = \frac{\mathcal{V}^*-\mathcal{V}^n}{\mathcal{V}^n\,\tau_{\mathcal{V}}}\int_{\Omega^n} q, \quad (50)$$

$$\frac{\partial\mathcal{E}_X^{n+1}}{\partial\mathbf{X}^{j,n+1}} - \left(\beta_f\,\boldsymbol{Y}^{j,n+1} \;-\; M^j\,\frac{\boldsymbol{Y}^{j,n+1}-\boldsymbol{Y}^{j,n}}{\delta t}\right) =$$
$$= \int_{\Upsilon^{j,n+1}}\left(\mathbf{f}^{\,{\rm con},\Upsilon,n+1}(\mathbf{x}^{\Upsilon,n+1}) + \mathbf{f}^{\,d,\Upsilon,n+1}(\mathbf{x}^{\Upsilon,n+1})\right), \quad (51)$$

with,

$$\mathcal{E}_X^{n+1} \;=\; \sum_{k=1}^{N_e}\left[\frac{k_BT\ell_m\,(3(x_k^{n+1})^2-2(x_k^{n+1})^3)}{4\ell_p(1-x_k^{n+1})} + \frac{k_p}{\ell_k^{n+1}}\right], \quad x_k^{n+1}=\ell_k^{n+1}/\ell_m, \quad (52)$$

$$\mathbf{f}^{\,{\rm con},\Gamma,n+1}(\mathbf{x}^{\Gamma,n+1}) = -\,\beta_\Gamma\int_{\Upsilon^{n+1}}\beta_\Upsilon\,\phi'(\|\mathbf{x}^{\Gamma,n+1}-\mathbf{x}^{\Upsilon,n+1}\|)\,\frac{\mathbf{x}^{\Gamma,n+1}-\mathbf{x}^{\Upsilon,n+1}}{\|\mathbf{x}^{\Gamma,n+1}-\mathbf{x}^{\Upsilon,n+1}\|}, \quad (53)$$

$$\mathbf{f}^{\,{\rm con},\Upsilon,n+1}(\mathbf{x}^{\Upsilon}) = \;\beta_\Upsilon\int_{\Gamma^{n+1}}\beta_\Gamma\,\phi'(\|\mathbf{x}^{\Gamma,n+1}-\mathbf{x}^{\Upsilon,n+1}\|)\,\frac{\mathbf{x}^{\Gamma,n+1}-\mathbf{x}^{\Upsilon,n+1}}{\|\mathbf{x}^{\Gamma,n+1}-\mathbf{x}^{\Upsilon,n+1}\|}, \quad (54)$$

$$\mathbf{f}^{d,\Upsilon,n+1}(\mathbf{x}^{\Upsilon,n+1}) = \int_{\Gamma^{n+1}}\eta\left(\boldsymbol{w}_h^{n+1}(\mathbf{x}^{\Gamma,n+1}) - \frac{\mathbf{x}^{\Upsilon,n+1}-\mathbf{x}^{\Upsilon,n}}{\delta t}\right), \quad (55)$$

$\forall\,(\boldsymbol{z},\xi,\boldsymbol{\zeta},q)\;\in\;\boldsymbol{W}_h^n\times Q_h^n\times\boldsymbol{K}_h^n\times\mathcal{P}_h^n$.

We need to provide some notes to comment the new stabilization term introduced and some generalizing additions compared to the evolutionary continuum model. The stabilization terms of the (48) and (50)

$$\int_{\Gamma^n}\gamma_h^{\mathcal{A}}\,(\nabla_\Gamma\,\sigma_h^{n+1}-\boldsymbol{g}_h^n)\cdot\,\nabla_\Gamma\xi, \quad (56)$$

$$\int_{\Omega^n}\gamma_h^{\mathcal{V}}\,(\nabla p_h^{n+1}-\boldsymbol{h}_h^n)\cdot\,\nabla q, \quad (57)$$

are similar; they aim to fix the checkerboard modes due to the equal order interpolation of $\boldsymbol{w}_h$, σ_h, and p_h, benefiting from the same idea of the works (see [55]), In the (56) and (57), $\gamma_h^{\dashv}$ and $\gamma_h^{\mathcal{V}}$ are parameters. Then $\boldsymbol{g}_h^n$ and $\boldsymbol{h}_h^n$ are the $L^2(\Gamma)$-projection of $\nabla_\Gamma\,\sigma_h^{n+1}$ onto $(Q_h^n)^3$ and $L^2(\Omega)$-projection of ∇p_h^{n+1} into $(\mathcal{P}_h^n)^3$ respectively, i.e.,

$$\int_{\Gamma^n}\boldsymbol{g}_h^n\cdot\boldsymbol{z} = \int_{\Gamma^n}\nabla_\Gamma\sigma_h^{n+1}\cdot\boldsymbol{z}, \quad \forall\boldsymbol{z}\in(Q_h^n)^3, \quad (58)$$

$$\int_{\Omega^n} \boldsymbol{h}_h^n \cdot \boldsymbol{z} = \int_{\Omega^n} \nabla p_h^{n+1} \cdot \boldsymbol{z}, \quad \forall \boldsymbol{z} \in (\mathcal{P}_h^n)^3. \tag{59}$$

In equations (48) and (50) is heuristically verified that the characteristic times $\tau_{\mathcal{A}}$ and $\tau_{\mathcal{V}}$ can be set equal to $10\,\delta t$.

The other stabilization term concerns the Laplace-Beltrami equation (49); it is

$$-\int_{\Gamma^n} \tau_k \, \nabla_\Gamma \boldsymbol{w}_h^{n+1} \, : \, \nabla_\Gamma \boldsymbol{\zeta} \tag{60}$$

as provided by Bänsch [56] to increase the temporal stability. Rodrigeus et al. [24] suggest to set $\tau_k = \delta t$.

Furthermore, the equation (51) concerning the cytoskeelton dynamics was integrated with the component

$$\beta_f \, \boldsymbol{Y}^{j,n+1} \; - \; M^j \, \frac{\boldsymbol{Y}^{j,n+1} - \boldsymbol{Y}^{j,n}}{\delta t} \tag{61}$$

to allow the introduction of: (i) a friction term, being β_f a constant parameter, and (ii) the inertial effect due to the M^j masses of the cytoskeleton junctions. In the following results, we consider these masses negligible, but the complete model can be numerically integrated with an implicit Newmark scheme and solved by a Newton-Raphson iterative procedure. Let us proceed to validate the computational formulation of the model through numerical tests.

3.2 Equilibrium and resting shape

We opt to use a relaxing process to test our computational formulation. This virtual experiment consists in letting the system tend to a minimum of energy (condition of equilibrium) without applying any external force. This test has a value both from a mathematical point of view to evaluate the numerical consistency of the model, but also from a physical/biological point of view. In the case of the red blood cell, in fact, the resting form of the cell, which in healthy conditions has the well-known biconcave physiognomy, is closely related to its biological functionality. However, various states and forms of disease can give different morphologies to the red blood cell, with mechanical and physiological implications of various kinds. An example of a sample of diseased red blood cells seen under a microscope is shown in Figure 3.

To compare the model with the results presented in the literature, let us consider a sphere of radius $r = 3.27\mu m$ as the reference form, as in the works of [58, 20]. In such case, the sphere surface area and volume are $A_{sphere} = 134.3709$ and $V_{sphere} = 146.4643$, respectively. We suppose to gradually reduce the volume to a target value V_{target}, defining a reduced volume parameter as

$$v_{reduced} = \frac{V_{target}}{4/3\pi r^3}. \tag{62}$$

According to the benchmarking values, a reduced volume $v_{reduced} \approx 0.60$ corresponds to the classical biconcave shape; but this depends also on the possible variation of the area. For detailed studies of the resulting equilibrium shapes, we refer the reader to the articles of [59, 57]

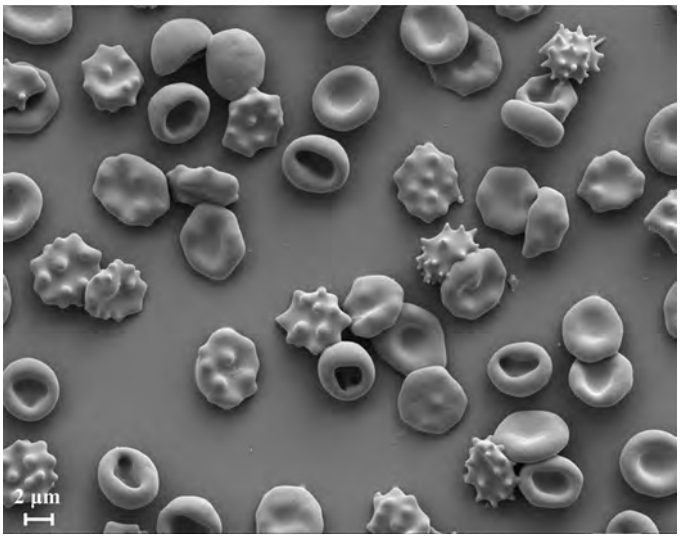

Figure 3: Heterogeneous sample of RBCs affected by stomatocytosis and echinocytosis under the scanning electron microscope and reported on https://doi.org/10.1371/journal.pone.0215447.g001 [57].

In our case, we refer to the parameters setup listed in Table 2 for all the model components, to solve our discrete model of equations (45) – (55). In the following test, we have introduced a cytoskeleton of 741 nodes of radius $R = 0.05$ and a cytoplamatic internal fluid of viscosity $\mu_f = 0.01$.

Table 2: Setup of parameters of the relaxation process simulations.

Value	**Symbol**	**Description**	**Component**
1.0	$k_B\,T$	energy unit	(WLC)
2	n	POW exponent	(WLC)
1.0	β_Γ	bilayer interaction constant	(INT)
1.0	β_Υ	cyto interaction constant	(INT)
6	k	LJ potential coefficient	(INT)
200	ε	Interaction strength constant	(INT)
0.05	r_0	equilibirum cyto-membrane distance	(INT)
0.05	R	radius of cyto-sphere	(INT)
1.0	μ	bilayer viscosity	(BIL)
20.0	C_{ch}	Canham constant	(BIL)
118.270	A_{target}	target RBC surface area	(BIL)
67.747	V_{target}	target RBC volume	(BIL)
0.01	μ_f	fluid viscosity	(FLUID)

The safe red blood cell biconcave morphology is obtained. As we can see from Figure 4, the biconcavity is particularly accentuated, due to a significant reduction in the target volume. The nodes of the cytoskeleton are visualized to scale and the peculiar structure of

the junction complexes can be seen, with the spectrins colored according to their tension. The internal fluid reaches a substantially uniform pressure, as expected. The results obtained are qualitatively consistent with those obtained with our two-component model presented in [25]. In particular, the resulting values of the main quantities are reported in Table 3.

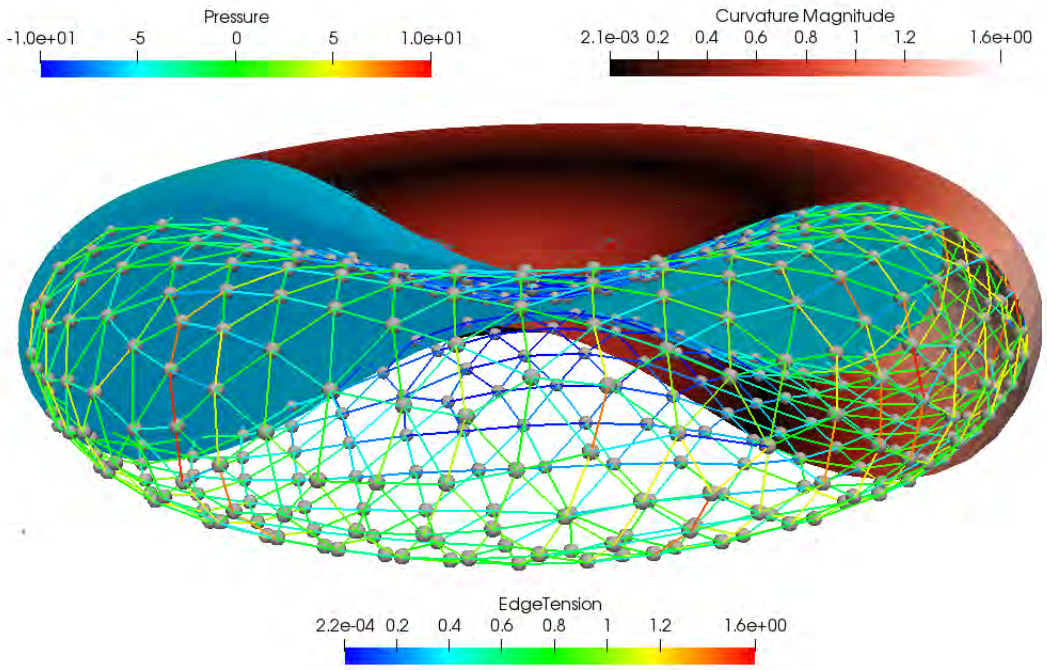

Figure 4: Snapshot of the RBC system after the relaxing process test described in the sub-section 3.2. The lipid bilayer is visualized in red scale according to the curvature magnitude. A section of the internal fluid is displayed in sky-blue, according to its pressure value. Indeed, the cytoskeleton network is plotted. The node size is in scale. The spectrin colors are referred to the edge tension.

Table 3: Quantities of numerical solutions the relaxation experiment of multi-component RBC model.

Case	$\mathcal{E}^{\Gamma}$	$\mathcal{E}_X$	$\mathcal{E}_{con}$	p
Biconcave relax	10.38×10^2	1.4×10^4	-5.6×10^1	-6.0

Following the same idea of the work of [20], we test the possibility to reach the prolate and stomatocyte shapes, imposing appropriate reduced volumes $v_{reduced}$ of 0.80 and 0.55 respectively. In Figure 5, we display with quantitative details the system configurations in both cases. We remark that, according to our calculations, the internal cytoplasmatic pressure in the prolate case is positive. Such results need to be verified in terms of biological consistency.

The morphological RBCs change is a very interesting topic from a mechanical point of view. It is known that, during the transition from the normal discoid shape to an abnormal

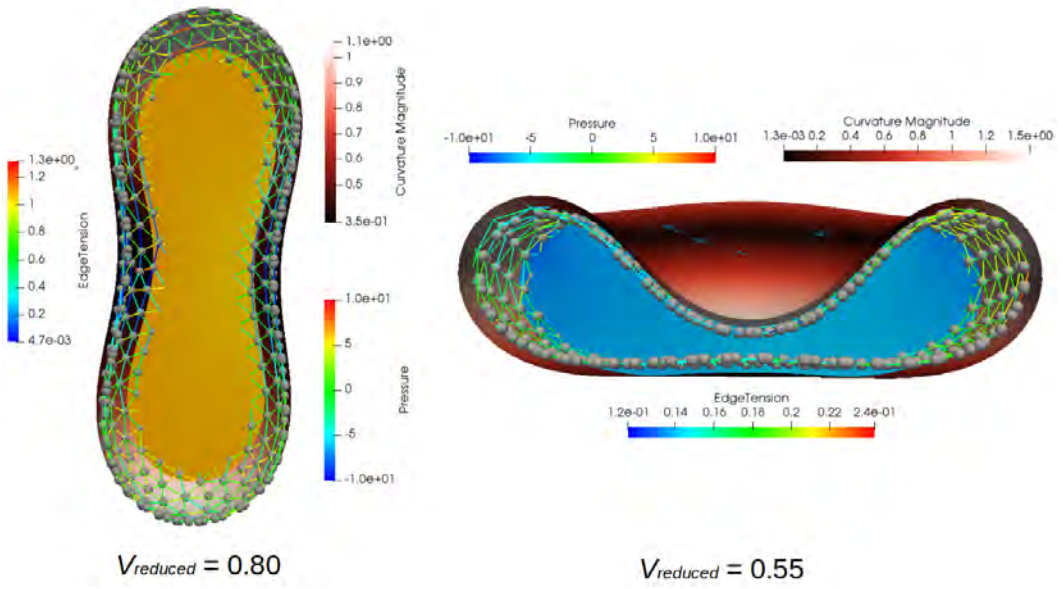

Figure 5: Snapshots of the RBC system reproducing the prolate and stomatocyte shapes, occurring imposing a reduce volumes $v_{reduced}$ of 0.80 and 0.55 respectively.

shape, the membrane shear, area, and bending moduli undergo significant variations [60]. The range of morphological irregularities of red blood cells is very wide [61, 62]. Specific applications of the model on this type of variants can lead to evaluate measurements and interactions for an eventual characterization of the membrane irregularities. In Figure 6 we show some main cases obtained with our code. The system configurations presented in this paper are available in the GitHub repository `https://github.com/LucaMeacci/RBCshapesMultiComponentModel` and can be visualized with the paraView open-source application.

We conclude this section with a final remark. The relaxing process is important also because it is related to the ability of the RBC to recover its original shape. It is proven that the characteristic time for the resting shape is within the range of $0.1-0.3$ [64, 65, 66].

If the virtual experiment of system relaxation can be considered useful for the verification of the computational formulation, on the other hand, we can better appreciate the characteristics of the multi-component model in simulations that foresee transitory states. For this reason, in the following section, we present a case of cell stretching with optical tweezers.

3.3 Stretching by optical tweezers

We aim in this section to show the potential of the multi-component model when used to study dynamic processes. The optical tweezers instrument provides for the possibility of stretching a RBC by two opposite beads attached to the bilayer. Being optical controlled, the beads can deform the RBC by applying a certain force. In Figure 7 we can see how the RBC results at a certain time during this process, using our code to mimic the experiment. It is possible to study the RBC response with respect to the force applied.

Figure 6: Acanthocyte, elliptocyte, teardrop cell, and spherocyte example obtained with the code. The source of the photo under the microscope is [63]

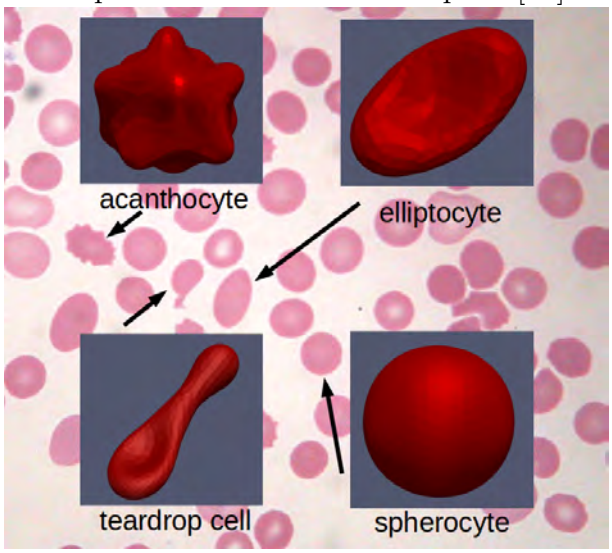

However, our multi-component model allows us to consider other details. Not only the external deformation and curvature distribution but the internal RBC behavior can be simulated. Figure 8 display the configuration of the internal cytoskeleton, that being attached to the lipid bilayer is affected and contributes to the global deformation. We can observe that the junction complexes closed to the regions attached by the beam present the spectrins in over-tension. This fact is due to the force that the cytoskeleton receives in the form of anchoring from the bilayer, through the interaction component of the model. Moreover, the cytoplasm dynamics are not trivial. Unlike the previous relaxation experiment, in this case, the fluid is not in a rest state. As we can see in the plot of Figure 9, the cytoplasm pressure does not result to be homogeneous. In the volume most prone to stretching and in the zone subject to folding, a non-trivial pressure distribution is shown.

The model, considering each component as a distinct entity, allows us to study the interaction phenomena between the parts, such as the detachment and reattachment of the cytoskeleton to the bilayer. Such effects are still to be fully understood and for this reason are of great interest; considered only in the most recent and advanced models available [65].

In particular, the internal fluid viscosity is a sensitive parameter that affects the results. With the same longitudinal elongation in the graph of Figure 10 we show how the RBC transversal diameter D_T evolves considering a fluid viscosity μ_f that varies from 0.01 to 10. The panels of Figure 11 display the extreme case and highlight as during the deformation, not only as naturally expected, the internal pressure values are significant different, but the RBC shape profile is notably dissimilar.

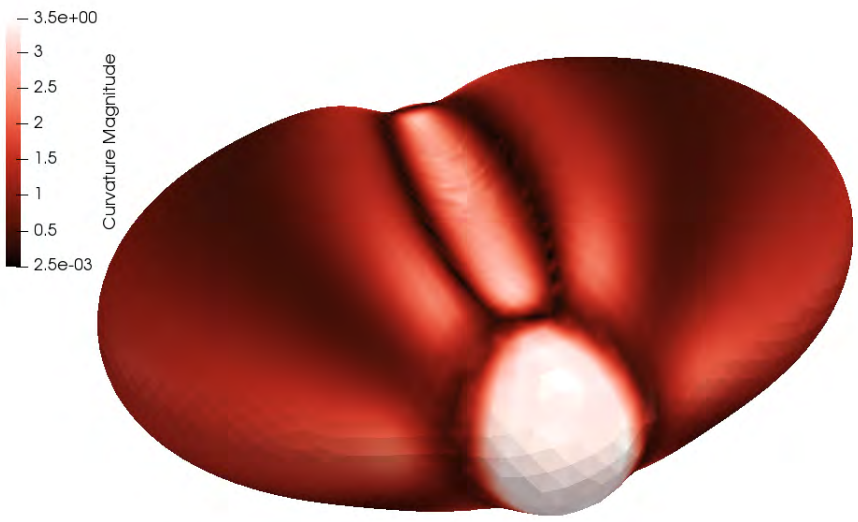

Figure 7: Visualization of the lipid bilayer at a certain instant during the optical tweezers stretching. The surface is colored on red scale according to the curvature magnitude.

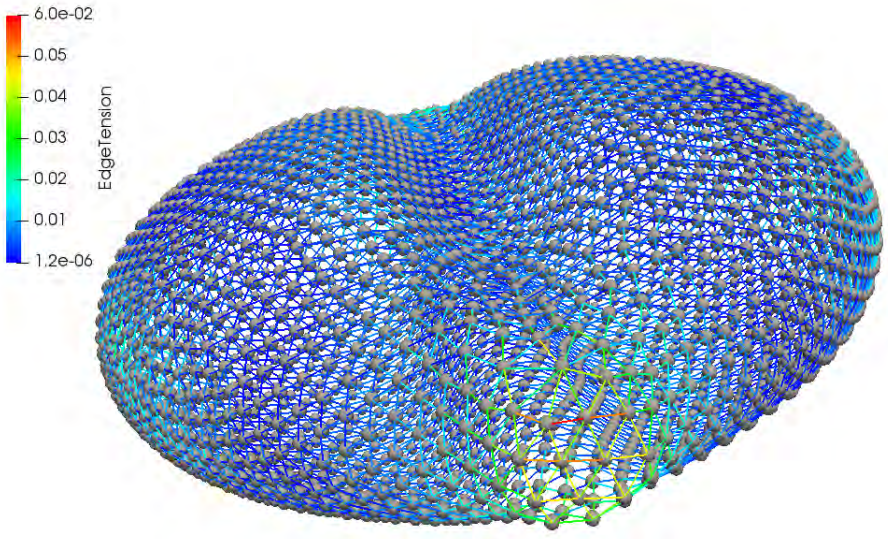

Figure 8: Visualization of the cytoskeleton at a certain instant during the optical tweezers stretching. The edges are colored based on its tensions.

3.3.1 Validation through experimental measurements

An optical tweezers experiment is a "testbed" to evaluate the deformation characteristics of the red blood cell during the dynamic process. We aim to compare the transient characteristics of the virtual red blood cell modeled with our model with the experimental measurements in the laboratory and the best practices generated by other mathematical models present in the literature. To this end, we introduce the quantities corresponding to the relative diameters increase (in the elongation phase). Let us consider to denote with

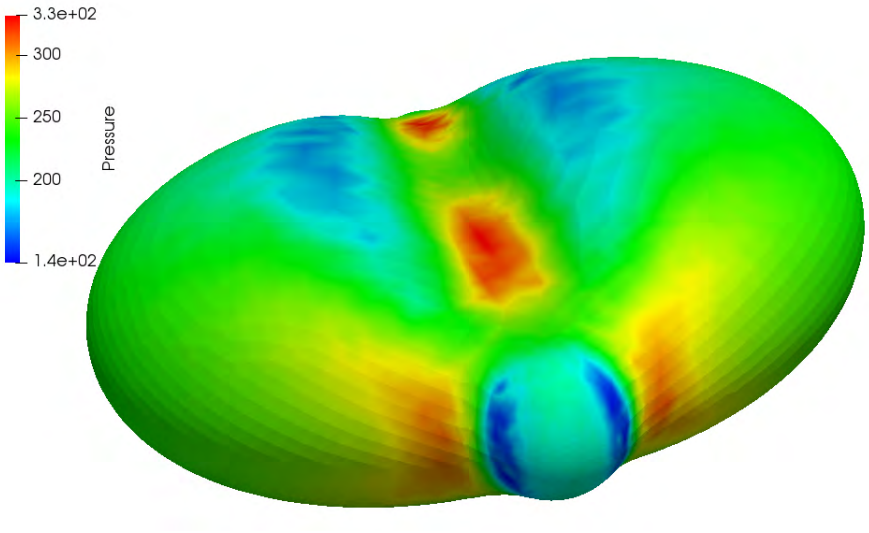

Figure 9: Visualization of the internal RBC fluid at a certain instant during the optical tweezers stretching. The fluid is colored according to its local pressure.

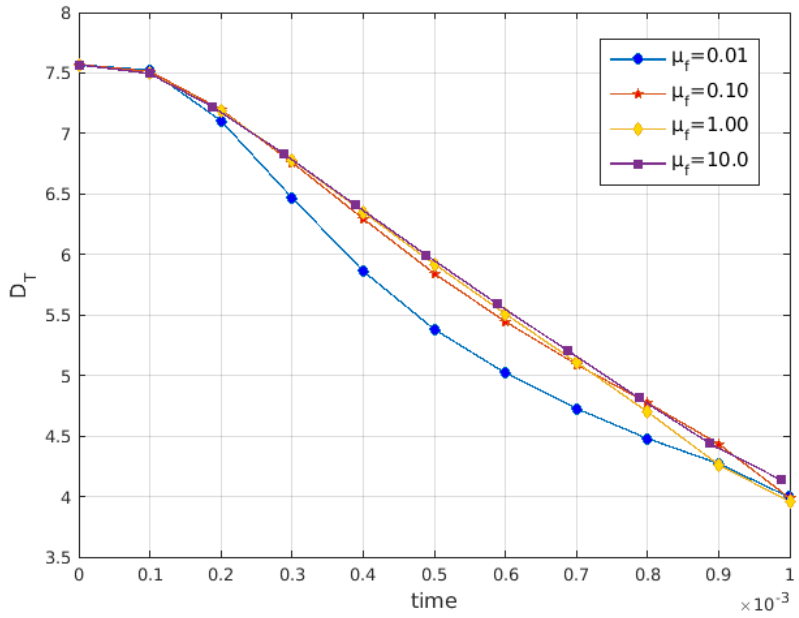

Figure 10: Trasversal RBC diameter D_T over the time, for a constant velocity of longitudinal elongation, under various cases of internal fluid viscosity μ_f.

D_a and D_t the longitudinal and transverse diameters with respect to the velocity direction of the optical tweezers, respectively. We define the longitudinal D_a^r and transverse strain D_t^r as follows

$$D_a^r = (D_a - D_a^0)/D_a^0, \qquad D_t^r = (D_t - D_t^0)/D_t^0\,, \tag{63}$$

with superscript 0 referring to the initial dimension.

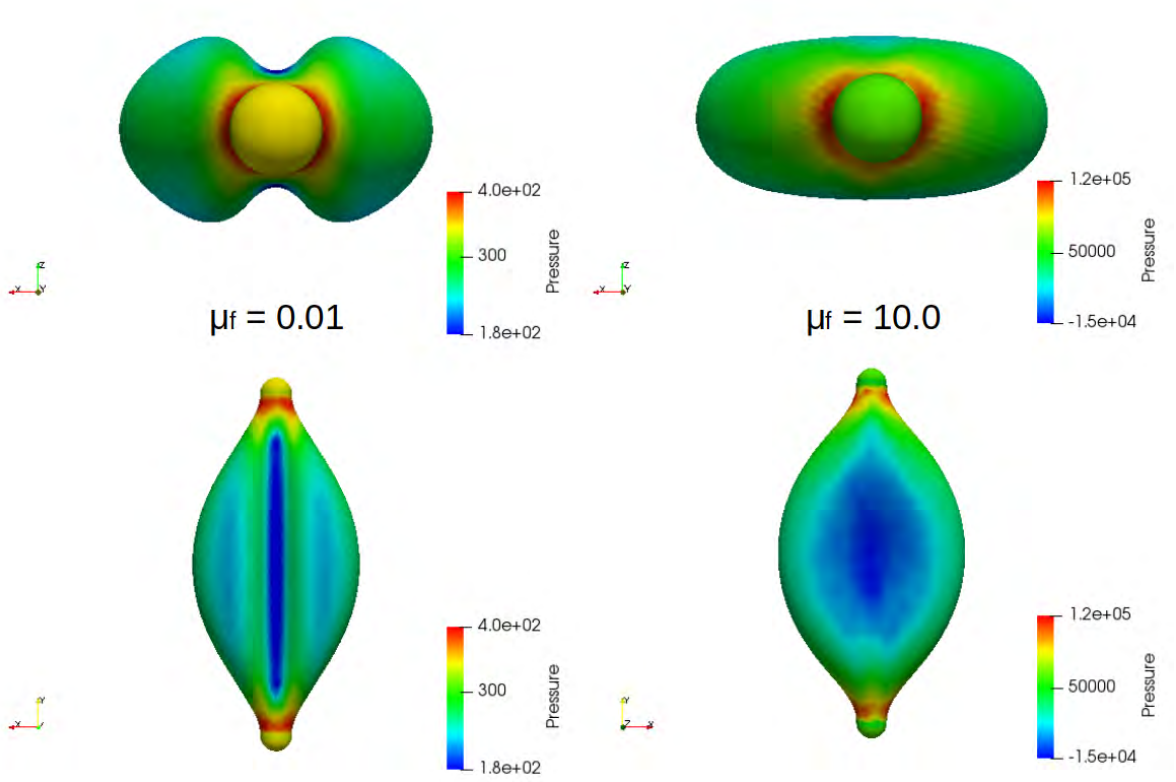

Figure 11: Trasversal RBC diameter D_T over the time, for a constant velocity of longitudinal elongation, under various cases of internal fluid viscosity μ_f.

Li and Liu [67] provided an experimental nanomechanical characterization of red blood cells by applying stretching forces via optical tweezers. They have measured the cell deformation directly from microscopic digital images over a set of cell samples. They have considered five RBC samples with an original radius ranging from 2.87 μm to 3.31 μm. In Figure 12, we plot the corresponding relative strains. For the reader's reference, we list the measurements in Table 4.

Other experimental/computational works concerning the stretching response of healthy and defective RBC can be considered to validate our model. In particular, we consider the results of the group of Suresh, Chang and Karniadakis [65, 68], considering the average values of the relative strains of a healthy and infected RBC with the malaria parasite *plasmodium falciparum*. As we can see in Figure 12 and Table 4, an evident effect due to the parasitization by P. falciparum is a significant increase in the elastic stiffness. In the data, this fact is reflected in greater transverse stretching than a fixed longitudinal elongation.

Concerning our computational simulation scaling, we follow the similar setup of the previous simulations. In particular, we consider an energy unit $k_B T = 1$, a Canham constant $C_{ch} = 20$, and an interaction strength constant $\epsilon = 5000$. The cytoskeleton consists of a network of around 750 nodes of radius 0.05. We remark that the internal viscosity of a RBC is five times higher than plasma, i.e., $6 \times 10^{-3} Pa \cdot s$ [69], so that considering our length scale of 1 μm it leads to set $\mu_f = 0.6$. During the virtual experiment, we consider

an opposite velocity of each micro-bead of $200\mu m$ with respect to the unit time.

With the aim of evaluating the multi-component contribution of the model, we proceed to simulate the experiment by the degree of completeness: (i) assuming only the lipid bilayer component, (ii) inserting the cytoskeleton, and finally (iii) also including the cytosol. For generality purpose, we also considered two cases of small (RBC1) and large (RBC2) RBCs of radius $2.85\,\mu m$ and $3.78\,\mu m$, respectively. In Table 4, we report our results and we compare them with the other data in Figure 12.

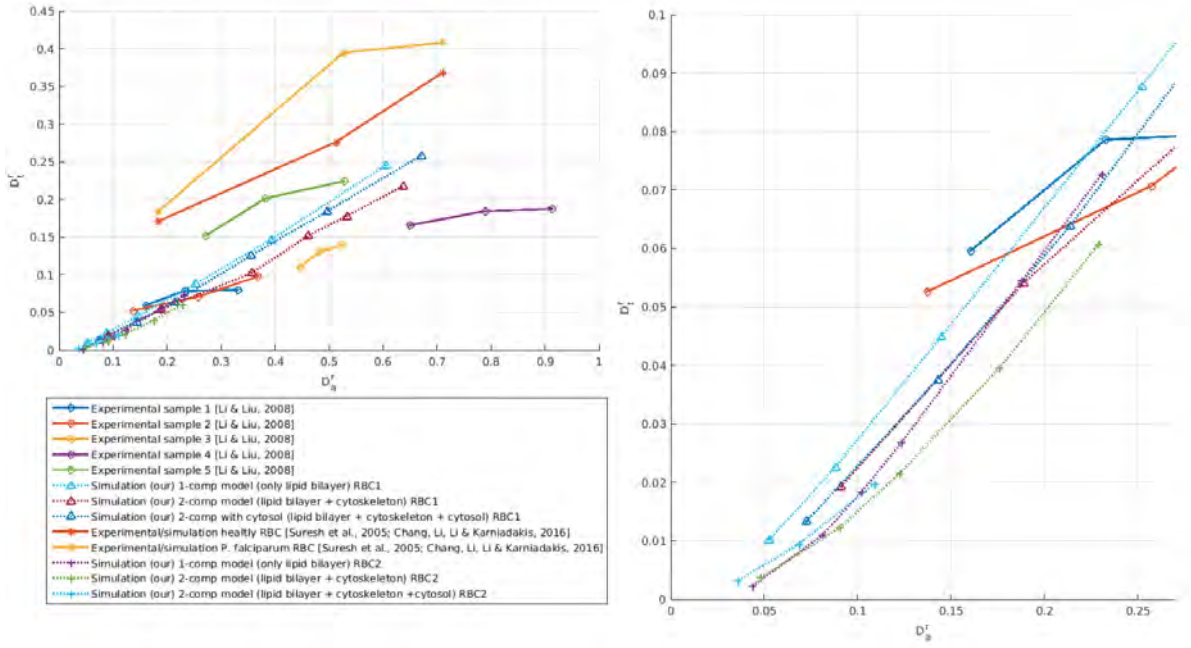

Figure 12: Comparison between experimental data and our numerical results.

Comparing our simulation results with the other data, as we can observe on the left panel of Figure 12, they reside within the variability window of the results described in the literature. In general, the transverse deformation grows monotonically with respect to the longitudinal deformation with a certain slope and with a slight tendency to a convex growth. On the other hand, by the zoom shown on the right panel, we can highlight some different responses with respect to the physical components considered. Our results show that the presence of the cytoskeleton softens the growth of the curve. Such behaviour is physically consistent, being that the lipid bilayer, intrinsically fluid in character, requires stabilization by association with an underlying cytoskeleton [70]. Considering the introduction of the internal fluid, from the trend of the graph, it seems that the absence of the cytosol affects only relatively the RBC deformation. Moreover, comparing the 2-component model with and without internal fluid, the results indicate that for a fixed longitudinal elongation, the corresponding transverse diameter is slightly less in presence of the cytosol. This result, which may appear to be counter-intuitive, is explained by the behavior with respect to the axis perpendicular to the plane between the two diameters. In Figure 13, we display the transient configuration of the system, coloring the outer bilayer according to the magnitude of its curvature. The images suggest a visible difference between the two configurations. Without the cytosol, the center of

the biconcave disc digs less spherically, tending to make the fold of the membrane stretch towards the microbeads. Such an effect is concomitantly reflected on the velocity field profile of the bilayer, which in the same central disk region in the case with cytosol it is on average lower than the case without cytosol. We remark that the internal pressure field in the cytosol case is not homogeneous and assumes a corresponding behavior. We can appreciate also the local influence on the pressure of the cytosol due to the presence of the nodes of the cytoskeleton.

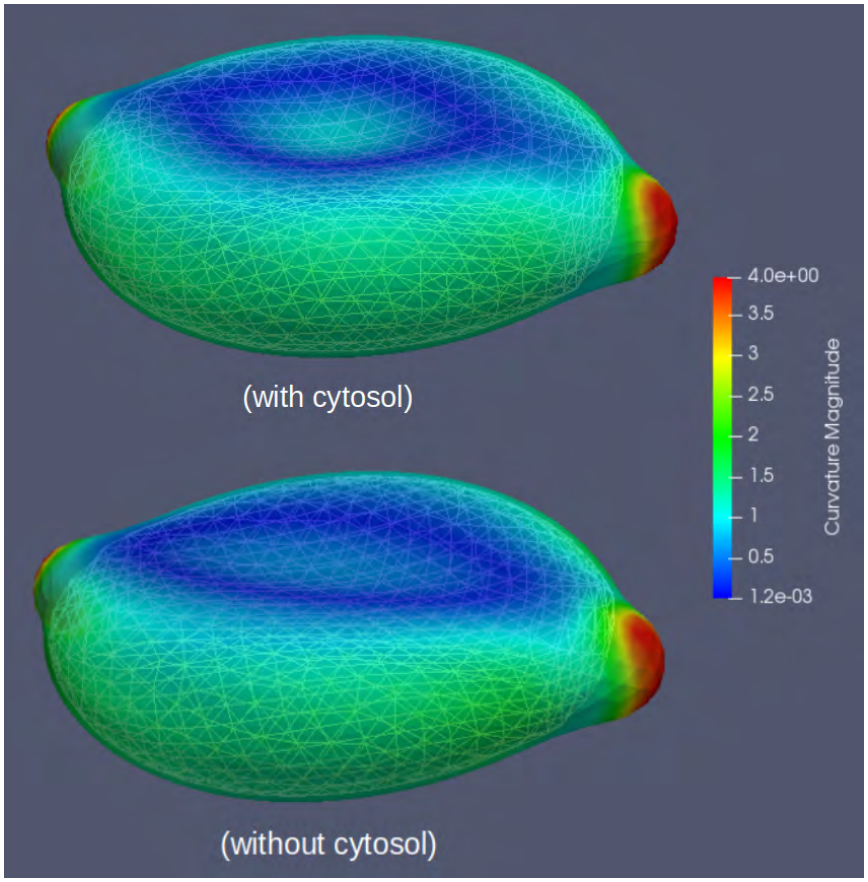

Figure 13: Visualization of our simulation configuration of the RBC1 at a fixed time during the stretching process, performed by our model with and without cytosol.

The cytosol ability to avoid that the fold crosses for the entire longitudinal diameter appropriately illustrates how the cytosol serves to maintain the cell volume and precludes contact between different parts of the cell [28].

We finally remark that we have found a certain discord in our simulations on the possibility that a cytoskeleton of an inactive nature (without the ability to rearrange itself) can remain anchored to the bilayer for important efforts such as those present in the work of Chang et al. [65]. Nonetheless, we agree that spectrin detachment events are relatively infrequent and appear in extreme cases [65, 71]. Furthermore, the formation of blebs (balloon-shaped membrane protrusions with no cytoskeleton content) turns out to be a possible phenomenon with physiological and mechanical implications [72, 73]. Our simulation results reinforce the idea that stress causes membrane rearrangements to adapt

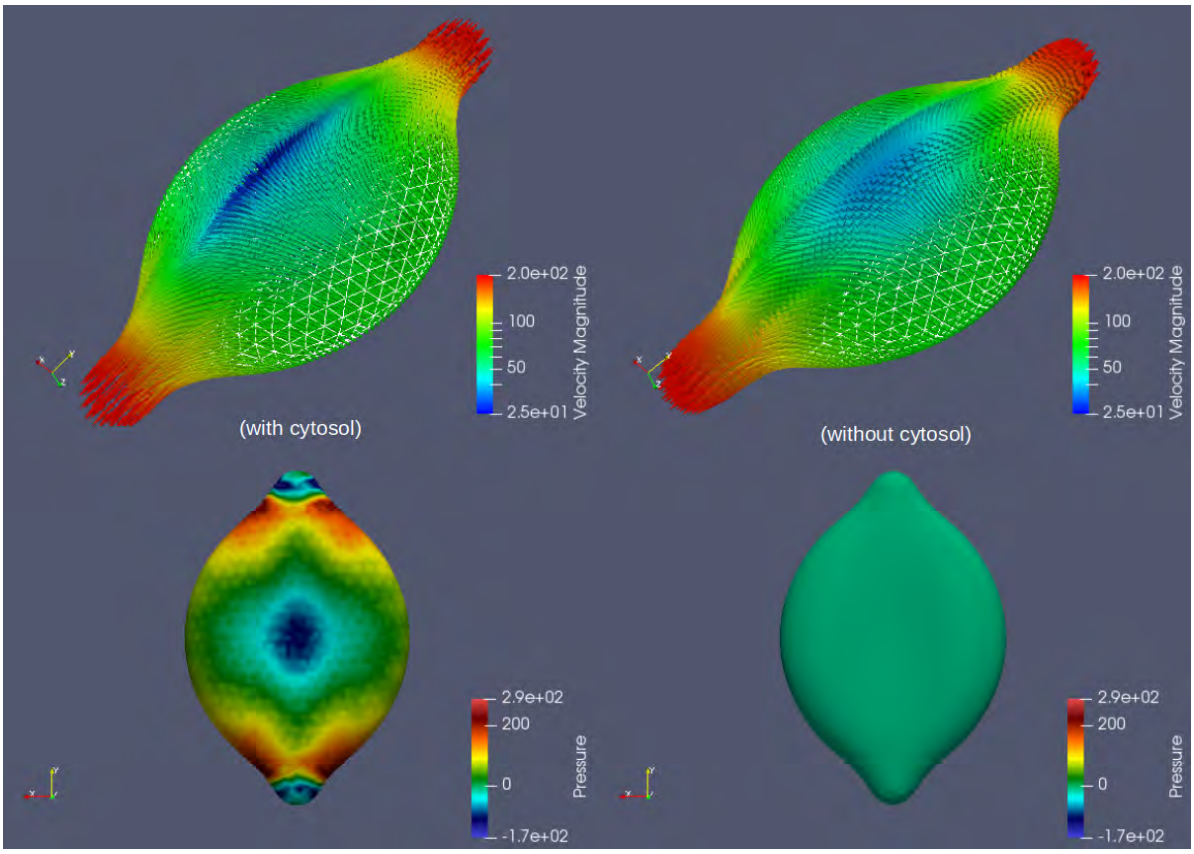

Figure 14: Visualization of lipid bilayer velocity field and cytosol pressure field of the RBC1 at a fixed time during the stretching process, performed by our model with and without cytosol.

to the load and, in particular, that the cytoskeleton is dynamic and can rapidly adapt to major changes in the cell shape [74, 75, 76]. Another speculative explanation is that the effective energy unit k_BT should be reduced, resulting in a lower cytoskeleton stiffness (see [77]). In Figure 15, we show a zoom on the RBC of how the cytoskeleton can follow the membrane movement included in the region adjacent to the stretching due to the bead.

4 Conclusions

In this paper, a new mathematical/computational formulation for a multi-component red blood cell model was presented. The emphasis of the work is centered on the possibility of performing the mathematical modeling of the following RBC components: (i) the lipid bilayer behavior, (ii) the cytoskeleton dynamics, (iii) the interaction activity between them, and (iv) the internal cytoplasm flow. Furthermore, the model considers a continuous definition of the lipid bilayer, allowing to use finite element methods. The text contains a detailed description of the construction of the model and its mathematical well-posedness, and it is tested with virtual experiments to show the potential and

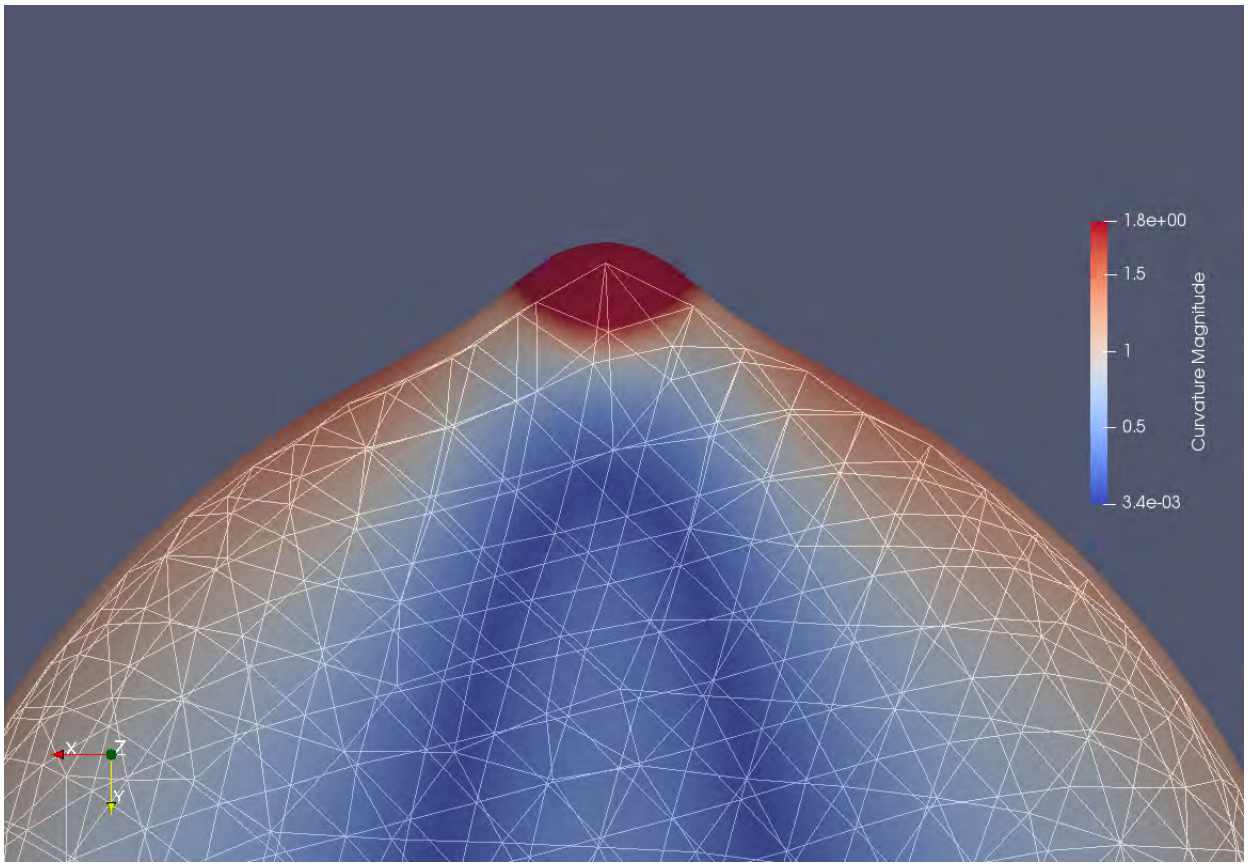

Figure 15: Detail of the adhesive cyto-bilayer movement during optical stretching experiment with weakened cytoskeleton ($k_BT = 10^{-3}$).

advantages deriving from its implementation. Numerous studies and applications can be developed, implementing simulations on the basis of experimental observations.

Declaration of competing interests

The authors declare that they have no known competing financial interests or personal relationships that could have appeared to influence the work reported in this paper.

Acknowledgements

The work was supported by grants from the INCT-MACC (Instituto Nacional de Ciência e Tecnologia - Medicina Assistida por Computação Científica), approved from CNPq (Conselho Nacional de Desenvolvimento Científico e Tecnológico) of Brazil and financed by FAPESP (Fundação de Amparo à Pesquisa do Estado de São Paulo) of Brazil (Grant 2014/50889-7). This research was developed making use of the computational resources (Euler cluster) of the CeMEAI (Center for Mathematical Sciences Applied to Industry) financed by FAPESP of Brazil (Grant 2013/07375-0). L.M. acknowledges the Foundation

CAPES (Coordenação de Aperfeiçoamento de Pessoal de Nível Superior) of the Ministry of Education of the Federal Republic of Brazil for economic support (Grant PROEX-9740044/D). L.M. sincerely thanks Arantxa Deneb Gómez Pirela for the art of the Figure 1.

References

[1] S. E. Lux, "Anatomy of the red cell membrane skeleton: unanswered questions," *Blood*, vol. 127, no. 2, pp. 187–199, 2016.

[2] X. Li, H. Lu, and Z. Peng, "Continuum-and particle-based modeling of human red blood cells," *Handbook of Materials Modeling: Applications: Current and Emerging Materials*, pp. 2593–2609, 2020.

[3] J. B. Freund, "Numerical simulation of flowing blood cells," *Annual review of fluid mechanics*, vol. 46, pp. 67–95, 2014.

[4] M. Ju, S. S. Ye, B. Namgung, S. Cho, H. T. Low, H. L. Leo, and S. Kim, "A review of numerical methods for red blood cell flow simulation," *Computer methods in biomechanics and biomedical engineering*, vol. 18, no. 2, pp. 130–140, 2015.

[5] D. Barthes-Biesel, "Motion and deformation of elastic capsules and vesicles in flow," *Annual Review of fluid mechanics*, vol. 48, pp. 25–52, 2016.

[6] S. Ramanujan and C. Pozrikidis, "Deformation of liquid capsules enclosed by elastic membranes in simple shear flow: large deformations and the effect of fluid viscosities," *Journal of Fluid Mechanics*, vol. 361, p. 117–143, 1998.

[7] S. K. Veerapaneni, A. Rahimian, G. Biros, and D. Zorin, "A fast algorithm for simulating vesicle flows in three dimensions," *Journal of Computational Physics*, vol. 230, no. 14, pp. 5610–5634, 2011.

[8] A. Z. K. Yazdani and P. Bagchi, "Phase diagram and breathing dynamics of a single red blood cell and a biconcave capsule in dilute shear flow," *Phys. Rev. E*, vol. 84, p. 026314, Aug 2011.

[9] A. Heintz, "A numerical method for simulation dynamics of incompressible lipid membranes in viscous fluid," *Journal of Computational and Applied Mathematics*, vol. 289, pp. 87–100, 2015.

[10] H. Li, H. Chang, J. Yang, L. Lu, Y. Tang, and G. Lykotrafitis, "Modeling biomembranes and red blood cells by coarse-grained particle methods," *Applied Mathematics and Mechanics*, vol. 39, no. 1, pp. 3–20, 2018.

[11] H. Noguchi and G. Gompper, "Shape transitions of fluid vesicles and red blood cells in capillary flows," *Proceedings of the National Academy of Sciences*, vol. 102, no. 40, pp. 14159–14164, 2005.

[12] J. L. McWhirter, H. Noguchi, and G. Gompper, "Flow-induced clustering and alignment of vesicles and red blood cells in microcapillaries," *Proceedings of the National Academy of Sciences*, vol. 106, no. 15, pp. 6039–6043, 2009.

[13] H. Li and G. Lykotrafitis, "Two-component coarse-grained molecular-dynamics model for the human erythrocyte membrane," *Biophysical journal*, vol. 102, no. 1, pp. 75–84, 2012.

[14] I. V. Pivkin and G. E. Karniadakis, "Accurate coarse-grained modeling of red blood cells," *Physical review letters*, vol. 101, no. 11, p. 118105, 2008.

[15] D. Fedosov, B. Caswell, and G. Karniadakis, "A multiscale red blood cell model with accurate mechanics, rheology and dynamics," *Biophys. J.*, vol. 98, pp. 2215–2225, 2010.

[16] Z. Peng, X. Li, I. V. Pivkin, M. Dao, G. E. Karniadakis, and S. Suresh, "Lipid bilayer and cytoskeletal interactions in a red blood cell," *Proceedings of the National Academy of Sciences*, vol. 110, no. 33, pp. 13356–13361, 2013.

[17] H. Li and G. Lykotrafitis, "Erythrocyte membrane model with explicit description of the lipid bilayer and the spectrin network," *Biophysical journal*, vol. 107, no. 3, pp. 642–653, 2014.

[18] Y.-H. Tang, L. Lu, H. Li, C. Evangelinos, L. Grinberg, V. Sachdeva, and G. E. Karniadakis, "Openrbc: a fast simulator of red blood cells at protein resolution," *Biophysical journal*, vol. 112, no. 10, pp. 2030–2037, 2017.

[19] S.-P. Fu, Z. Peng, H. Yuan, R. Kfoury, and Y.-N. Young, "Lennard-jones type pair-potential method for coarse-grained lipid bilayer membrane simulations in lammps," *Computer Physics Communications*, vol. 210, pp. 193–203, 2017.

[20] Z. Peng, R. J. Asaro, and Q. Zhu, "Multiscale simulation of erythrocyte membranes," *Physical Review E*, vol. 81, no. 3, p. 031904, 2010.

[21] Z. Peng, R. J. Asaro, and Q. Zhu, "Multiscale modelling of erythrocytes in stokes flow," *Journal of Fluid Mechanics*, vol. 686, p. 299, 2011.

[22] M. Arroyo and A. DeSimone, "Relaxation dynamics of fluid membranes," *Physical review E*, vol. 79, no. 3, p. 031915, 2009.

[23] J. W. Barrett, H. Garcke, and R. Nürnberg, "Numerical computations of the dynamics of fluidic membranes and vesicles," *Physical review E*, vol. 92, no. 5, p. 052704, 2015.

[24] D. S. Rodrigues, R. F. Ausas, F. Mut, and G. C. Buscaglia, "A semi-implicit finite element method for viscous lipid membranes," *Journal of Computational Physics*, vol. 298, pp. 565–584, 2015.

[25] L. Meacci, G. C. Buscaglia, F. Mut, R. F. Ausas, and M. Primicerio, "A new two-component approach in modeling red blood cells," *Communications in Applied and Industrial Mathematics*, vol. 11, no. 1, pp. 55–71, 2020.

[26] L. Meacci, G. C. Buscaglia, R. F. Ausas, and F. Mut, "A red blood cell cyto-bilayer interaction model," *Proceeding Series of the Brazilian Society of Computational and Applied Mathematics*, vol. 7, no. 1, 2020.

[27] H. Turlier, D. A. Fedosov, B. Audoly, T. Auth, N. S. Gov, C. Sykes, J.-F. Joanny, G. Gompper, and T. Betz, "Equilibrium physics breakdown reveals the active nature of red blood cell flickering," *Nature Physics*, vol. 12, no. 5, pp. 513–519, 2016.

[28] M. Dao, C. T. Lim, and S. Suresh, "Mechanics of the human red blood cell deformed by optical tweezers," *Journal of the Mechanics and Physics of Solids*, vol. 51, no. 11-12, pp. 2259–2280, 2003.

[29] S. K. Boey, D. H. Boal, and D. E. Discher, "Simulations of the erythrocyte cytoskeleton at large deformation. i. microscopic models," *Biophysical Journal*, vol. 75, no. 3, pp. 1573–1583, 1998.

[30] D. E. Discher, D. H. Boal, and S. K. Boey, "Simulations of the erythrocyte cytoskeleton at large deformation. ii. micropipette aspiration," *Biophysical Journal*, vol. 75, no. 3, pp. 1584–1597, 1998.

[31] D. Capecchi, *History of virtual work laws: a history of mechanics prospective*, vol. 42. Springer Science & Business Media, 2012.

[32] G. C. Buscaglia and R. F. Ausas, "Variational formulations for surface tension, capillarity and wetting," *Computer Methods in Applied Mechanics and Engineering*, vol. 200, no. 45-46, pp. 3011–3025, 2011.

[33] A. Biria, M. Maleki, and E. Fried, "Continuum theory for the edge of an open lipid bilayer," *Advances in Applied Mechanics*, vol. 46, pp. 1–68, 2013.

[34] M. Boussinesq, "Sur l'existance d'une viscosite superficielle, dans la mince couche de transition separant un liquide d'une autre fluide contigue," *Ann. Chim. Phys*, vol. 29, pp. 349–357, 1913.

[35] L. Scriven, "Dynamics of a fluid interface equation of motion for newtonian surface fluids," *Chemical Engineering Science*, vol. 12, no. 2, pp. 98–108, 1960.

[36] S. Gross and A. Reusken, *Numerical methods for two-phase incompressible flows*, vol. 40. Springer Science & Business Media, 2011.

[37] J. W. Barrett, H. Garcke, and R. Nürnberg, "A stable numerical method for the dynamics of fluidic membranes," *Numerische Mathematik*, vol. 134, no. 4, pp. 783–822, 2016.

[38] P. B. Canham, "The minimum energy of bending as a possible explanation of the biconcave shape of the human red blood cell," *Journal of theoretical biology*, vol. 26, no. 1, pp. 61IN777–76IN881, 1970.

[39] W. Helfrich, "Elastic properties of lipid bilayers: theory and possible experiments," *Zeitschrift für Naturforschung C*, vol. 28, no. 11-12, pp. 693–703, 1973.

[40] A. Bonito, R. H. Nochetto, and M. S. Pauletti, "Parametric fem for geometric biomembranes," *Journal of Computational Physics*, vol. 229, no. 9, pp. 3171–3188, 2010.

[41] N. Mohandas and P. G. Gallagher, "Red cell membrane: past, present, and future," *Blood*, vol. 112, no. 10, pp. 3939–3948, 2008.

[42] W. Gratzer, "The red cell membrane and its cytoskeleton.," *Biochemical Journal*, vol. 198, no. 1, p. 1, 1981.

[43] D. A. Fedosov, B. Caswell, and G. E. Karniadakis, "Coarse-grained red blood cell model with accurate mechanical properties, rheology and dynamics," in *2009 Annual International Conference of the IEEE Engineering in Medicine and Biology Society*, pp. 4266–4269, IEEE, 2009.

[44] L. Meacci, R. F. Ausas, F. Mut, V. di Bari, and G. C. Buscaglia, "Modeling a red blood cell cytoskeleton: insights, tips, and code," *To be published*.

[45] J. Hansen, R. Skalak, S. Chien, and A. Hoger, "An elastic network model based on the structure of the red blood cell membrane skeleton," *Biophysical journal*, vol. 70, no. 1, pp. 146–166, 1996.

[46] D. A. Fedosov, H. Lei, B. Caswell, S. Suresh, and G. E. Karniadakis, "Multiscale modeling of red blood cell mechanics and blood flow in malaria," *PLoS computational biology*, vol. 7, no. 12, p. e1002270, 2011.

[47] R. A. Sauer, "Computational contact formulations for soft body adhesion," *Advances in Soft Matter Mechanics*, p. 55, 2012.

[48] L. Freund and Y. Lin, "The role of binder mobility in spontaneous adhesive contact and implications for cell adhesion," *Journal of the Mechanics and Physics of Solids*, vol. 52, no. 11, pp. 2455–2472, 2004.

[49] E. Kuusela and W. Alt, "Continuum model of cell adhesion and migration," *Journal of mathematical biology*, vol. 58, no. 1-2, p. 135, 2009.

[50] I. Pajic-Lijakovic and M. Milivojevic, "Modeling analysis of the lipid bilayer–cytoskeleton coupling in erythrocyte membrane," *Biomechanics and modeling in mechanobiology*, vol. 13, no. 5, pp. 1097–1104, 2014.

[51] J. N. Israelachvili, *Intermolecular and surface forces*. Academic press, 2011.

[52] T. Kashiwabara, C. M. Colciago, L. Dedè, and A. Quarteroni, "Well-posedness, regularity, and convergence analysis of the finite element approximation of a generalized robin boundary value problem," *SIAM Journal on Numerical Analysis*, vol. 53, no. 1, pp. 105–126, 2015.

[53] A. Bonito, A. Demlow, and R. H. Nochetto, "Finite element methods for the laplace–beltrami operator," in *Handbook of Numerical Analysis*, vol. 21, pp. 1–103, Elsevier, 2020.

[54] F. Clément and V. Martin, "The lax-milgram theorem. a detailed proof to be formalized in coq," *arXiv preprint arXiv:1607.03618*, 2016.

[55] R. Codina, J. Blasco, G. C. Buscaglia, and A. Huerta, "Implementation of a stabilized finite element formulation for the incompressible navier–stokes equations based on a pressure gradient projection," *International Journal for Numerical Methods in Fluids*, vol. 37, no. 4, pp. 419–444, 2001.

[56] E. Bänsch, "Finite element discretization of the navier–stokes equations with a free capillary surface," *Numerische Mathematik*, vol. 88, no. 2, pp. 203–235, 2001.

[57] N. M. Geekiyanage, M. A. Balanant, E. Sauret, S. Saha, R. Flower, C. T. Lim, and Y. Gu, "A coarse-grained red blood cell membrane model to study stomatocyte-discocyte-echinocyte morphologies," *PloS one*, vol. 14, no. 4, p. e0215447, 2019.

[58] J. Li, M. Dao, C. Lim, and S. Suresh, "Spectrin-level modeling of the cytoskeleton and optical tweezers stretching of the erythrocyte," *Biophysical journal*, vol. 88, no. 5, pp. 3707–3719, 2005.

[59] U. Seifert, K. Berndl, and R. Lipowsky, "Shape transformations of vesicles: Phase diagram for spontaneous-curvature and bilayer-coupling models," *Physical review A*, vol. 44, no. 2, p. 1182, 1991.

[60] Y. Park, C. A. Best, K. Badizadegan, R. R. Dasari, M. S. Feld, T. Kuriabova, M. L. Henle, A. J. Levine, and G. Popescu, "Measurement of red blood cell mechanics during morphological changes," *Proceedings of the National Academy of Sciences*, vol. 107, no. 15, pp. 6731–6736, 2010.

[61] J. Ford, "Red blood cell morphology," *International journal of laboratory hematology*, vol. 35, no. 3, pp. 351–357, 2013.

[62] P. Ruef and O. Linderkamp, "Deformability and geometry of neonatal erythrocytes with irregular shapes," *Pediatric research*, vol. 45, no. 1, pp. 114–119, 1999.

[63] B. Key, "Diseases of red blood cells." urlhttps://basicmedicalkey.com/diseases-of-red-blood-cells/, 2016.

[64] R. M. Hochmuth, P. Worthy, and E. A. Evans, "Red cell extensional recovery and the determination of membrane viscosity," *Biophysical journal*, vol. 26, no. 1, pp. 101–114, 1979.

[65] H.-Y. Chang, X. Li, H. Li, and G. E. Karniadakis, "Md/dpd multiscale framework for predicting morphology and stresses of red blood cells in health and disease," *PLoS computational biology*, vol. 12, no. 10, p. e1005173, 2016.

[66] S. Tan and M. Xu, "Numerical studies of shape recovery of a red blood cell using dissipative particle dynamics," *International Journal of Computational Methods*, vol. 17, no. 07, p. 1950032, 2020.

[67] C. Li and K. Liu, "Nanomechanical characterization of red blood cells using optical tweezers," *Journal of Materials Science: Materials in Medicine*, vol. 19, no. 4, pp. 1529–1535, 2008.

[68] S. Suresh, J. Spatz, J. Mills, A. Micoulet, M. Dao, C. Lim, M. Beil, and T. Seufferlein, "Reprint of: connections between single-cell biomechanics and human disease states: gastrointestinal cancer and malaria," *Acta biomaterialia*, vol. 23, pp. S3–S15, 2015.

[69] C. Pozrikidis, "Numerical simulation of the flow-induced deformation of red blood cells," *Annals of biomedical engineering*, vol. 31, no. 10, pp. 1194–1205, 2003.

[70] D. Raucher, "Application of laser tweezers to studies of membrane–cytoskeleton adhesion," *Methods in cell biology*, vol. 89, pp. 451–466, 2008.

[71] R. Rodríguez-García, I. López-Montero, M. Mell, G. Egea, N. S. Gov, and F. Monroy, "Direct cytoskeleton forces cause membrane softening in red blood cells," *Biophysical journal*, vol. 108, no. 12, pp. 2794–2806, 2015.

[72] E. J. Spangler, C. W. Harvey, J. D. Revalee, P. S. Kumar, and M. Laradji, "Computer simulation of cytoskeleton-induced blebbing in lipid membranes," *Physical Review E*, vol. 84, no. 5, p. 051906, 2011.

[73] B. Pontes, N. Viana, L. Salgado, M. Farina, V. M. Neto, and H. Nussenzveig, "Cell cytoskeleton and tether extraction," *Biophysical journal*, vol. 101, no. 1, pp. 43–52, 2011.

[74] M. P. Sheetz, J. E. Sable, and H.-G. Döbereiner, "Continuous membrane-cytoskeleton adhesion requires continuous accommodation to lipid and cytoskeleton dynamics," *Annu. Rev. Biophys. Biomol. Struct.*, vol. 35, pp. 417–434, 2006.

[75] H. Li, J. Yang, T. T. Chu, R. Naidu, L. Lu, R. Chandramohanadas, M. Dao, and G. E. Karniadakis, "Cytoskeleton remodeling induces membrane stiffness and stability changes of maturing reticulocytes," *Biophysical journal*, vol. 114, no. 8, pp. 2014–2023, 2018.

[76] T. Avsievich, R. Zhu, A. Popov, A. Bykov, and I. Meglinski, "The advancement of blood cell research by optical tweezers," *Reviews in Physics*, vol. 5, p. 100043, 2020.

[77] R. Rodríguez-García, I. López-Montero, M. Mell, G. Egea, N. S. Gov, and F. Monroy, "Direct cytoskeleton forces cause membrane softening in red blood cells," *Biophysical journal*, vol. 108, no. 12, pp. 2794–2806, 2015.

Table 4: Experimental measurements and computational results on RBC deformation using optical tweezers. Our simulations are performed by 1-component (only lipid bilayer), 2-component (lipid bilayer and cytoskeleton) and 2-component with cytosol (lipid bilayer, cytoskeleton and internal fluid) models.

Test (sample)	Original radius (μm)	T. strain D_t^r	L. strain D_a^r
Li's exp. 1	2.96	0.0596	0.1605
		0.0786	0.2327
		0.0801	0.3314
Li's exp. 2	3.20	0.0526	0.1372
		0.0707	0.2574
		0.0979	0.3685
Li's exp. 3	2.87	0.1096	0.4456
		0.1309	0.4832
		0.1400	0.5240
Li's exp. 4	3.93	0.1656	0.6495
		0.1845	0.7891
		0.1875	0.9125
Li's exp. 5	3.31	0.1523	0.2722
		0.2014	0.3822
		0.2241	0.5273
Suresh & Karniadakis's healthy	3.80	0.1711	0.1842
		0.2763	0.5132
		0.3684	0.7105
Suresh & Karniadakis's P. falciparum	3.80	0.1842	0.1842
		0.3947	0.5263
		0.4079	0.7105
Our sim. 1-comp RBC1	2.85	0.0102	0.0526
		0.0226	0.0881
		0.0449	0.1447
		0.0877	0.2520
		0.1465	0.3927
		0.2449	0.6043
Our sim. 2-comp RBC1	2.85	0.0193	0.0912
		0.0540	0.1888
		0.1023	0.3570
		0.1516	0.4612
		0.1777	0.5321
		0.2175	0.6372
Our sim. 2-comp with cytosol RBC1	2.85	0.0133	0.0725
		0.0375	0.1428
		0.0639	0.2139
		0.1254	0.3553
		0.1842	0.4963
		0.2579	0.6702
Our sim. 1-comp RBC2	3.78	0.0022	0.0437
		0.0110	0.0811
		0.0184	0.1022
		0.0269	0.1235
		0.0545	0.1880
		0.0728	0.2308
Our sim. 2-comp RBC2	3.78	0.0037	0.0481
		0.0123	0.0907
		0.0215	0.1226
		0.0395	0.1758
		0.0607	0.2290
Our sim. 2-comp with cytosol RBC2	3.78	0.0032	0.0361
		0.0095	0.0686
		0.0197	0.1090